

Clustering of red and blue galaxies around high-redshift 3C radio sources as seen by the Hubble Space Telescope

Zohreh Ghaffari^{1,★}, Martin Haas¹, Marco Chiaberge², S. P. Willner³, Rolf Chini^{1,4}, Hendrik Hildebrandt¹, Michael West⁵, and Roberto de Propris⁶

¹ Astronomisches Institut, Ruhr-Universität Bochum, Universitätsstraße 150, 44801 Bochum, Germany

² Space Telescope Science Institute, 3700 San Martin Drive, Baltimore, MD 21218, USA

³ Center for Astrophysics | Harvard & Smithsonian, 60 Garden St., Cambridge, MA 02138, USA

⁴ Instituto de Astronomía, Universidad Católica del Norte, Avenida Angamos 0610, Casilla 1280 Antofagasta, Chile

⁵ Lowell Observatory, 1400 West Mars Hill Road, Flagstaff, AZ 86001, USA

⁶ Finnish Centre for Astronomy with the European Southern Observatory, University of Turku, Väisäläntie 20, 21500 Piikkiö, Finland

Received September, 2020; accepted, 2020

ABSTRACT

Galaxy surface density maps reveal the clustering of red and blue galaxies around 3C radio galaxies and quasars at $1 < z < 2.5$. The maps are made from optical and near-infrared *HST* images with a 2' field-of-view, where the filters encompass the 4000 Å break. 16 of 21 radio sources lie inside a galaxy overdensity of less than 250 kpc (30'') projected radius; the overdensity is defined as 3σ above the mean galaxy density of the periphery (30'' – 60''). We find a spatial galaxy segregation with brightness and color as well as evolution with redshift. At $z < 1.5$, the overdensity is dominated by red galaxies, while blue galaxies are more frequent in the periphery. With a few exceptions, the fainter galaxies contributing to the overdensity are bluer than the brighter galaxies. The derived number of central luminous red galaxies is comparable to that of the Coma cluster core. This and the brightness and color segregation of candidate cluster member galaxies leads us to conclude that at $1 < z < 1.5$ the 3C sources are not just becoming galaxy groups. Rather we suggest that the foundation of a galaxy cluster with luminous red galaxies has largely been set, and the formation of the red sequence is still going on from a reservoir of blue galaxies in the periphery. At $z > 1.5$, overdensities are less frequent and progressively composed of blue galaxies. Compared to $z < 1.5$, the lower galaxy concentration and bluer nature of potential cluster member galaxies indicate that a 3C cluster at $z > 1.5$ is in an earlier assembly phase. The clustering of galaxies around high-redshift 3C sources appears to precede with a few exceptions the assembly of detectable mass concentrations and of extended hot X-ray gas found for most of the lower-redshift 3C sources.

Key words. high-redshift — radio galaxies — clusters of galaxies

1. Introduction

Clusters of galaxies (henceforth simply called clusters) are the largest gravitationally bound structures in the Universe. Their formation and evolution is dominated by gravity, i.e., dark matter, while their large scale distribution and number density depends on the geometry of the Universe, i.e., dark energy. They contain several hundred to thousands of galaxies, while galaxy groups have only some dozen members. Young clusters are called proto-clusters. They are gravitationally bound but not yet compact nor virialized. For linguistic simplicity, we here do not distinguish between clusters and proto-clusters unless necessary. We distinguish between clusters in the nearby (or local) Universe (redshift $z < 0.2$), at intermediate distance ($z \sim 0.5$), at high redshift (high- z , $1 < z < 2.5$), and at very-high redshift beyond.

Clusters are most often recognised in the X-rays by their extended, hot intra-cluster gas or via the Sunyaev-Zel'dovich (SZ) effect allowing to infer the total mass. X-ray surveys found some dozen high- z clusters, for instance Fassbender et al. (2011); Mehrtens et al. (2012); Mantz et al. (2018). SZ surveys, for instance with the South Pole Telescope (SPT) (Carlstrom et al. 2011) including plenty of optical/NIR follow-up studies, have found thousands of new clusters but only a few dozen at $1 <$

$z < 1.5$ (Bleem et al. 2015; Hennig et al. 2017; Khullar et al. 2019; Huang et al. 2020). The *Planck* SZ cluster search projects so far found secure clusters up to $z \sim 0.85$ (Barrena et al. 2018; Aguado-Barahona et al. 2019; Barrena et al. 2020).

A possible reason for the scarcity of high- z X-ray or SZ cluster detections may be that the high- z clusters have not yet accumulated sufficient gaseous mass to be detectable with current instruments. The limitation for studying the cluster evolution becomes obvious at high redshift, where despite enormous efforts the detection of X-ray clusters or SZ clusters is challenging and rare compared to $z < 1$.

Clusters are as the name says characterised also by a clustering of galaxies. To find a clustering of galaxies in an early assembly phase, dedicated strategies are being explored, e.g., the search for enhancements of the galaxy surface density in wide field surveys and subsequent search for red sequences (RS), where the evolved red galaxies show up as a distinct line ("sequence") in color-magnitude diagrams (Gladders & Yee 2000). The *Spitzer Infrared Array Camera Shallow Survey* (Eisenhardt et al. 2004) identified 335 galaxy cluster and group candidates, 106 of which are at $z > 1$, and among which a few dozen candidates have been confirmed spectroscopically with $z \lesssim 1.5$ (Eisenhardt et al. 2008; Papovich et al. 2010). The *Spitzer Adaptation of the Red-Sequence Cluster Survey* (SPARCS) covered

* Corresponding author: ghaffari@astro.ruhr-uni-bochum.de

42 square degrees of the SWIRE fields. SPARCS combined shallow near- and mid-infrared images from the *Spitzer Space Telescope* with deep z -band imaging from the ground, finding numerous clusters at $z < 1$ but only about a dozen clusters at $1 < z < 1.6$ (Wilson et al. 2009; Muzzin et al. 2009; Hildebrandt et al. 2011). This again suggests that high- z clusters (with or without RS) exist but are rare compared to the numbers at low and intermediate redshift.

An alternative strategy to search for clusters at high and very-high redshift is reviewed by Miley & De Breuck (2008). Powerful radio galaxies (RGs) typically are massive galaxies over the entire redshift range; therefore they should mark cosmic mass concentrations and places of galaxy clusters. The main advantage of using the high- z RGs as mass beacons is that one already knows the redshift (of the RG) to search for cluster member galaxies. The high- z RGs indicate also an extremely powerful black hole and star forming activity, which is often triggered by mergers (Chiaberge et al. 2015). The upper end of activity level implicitly provides an additional selection criterion, whereby merger-food galaxies are present as well as sufficient circumgalactic medium acting as working surface for the radio jets and lobes. One may speculate that the environment of high- z RGs should be comparable over a large redshift range. This opens the possibility to fairly study the evolution of the anticipated cluster assembly. This is by itself interesting, irrespective of the issue of what one may conclude for cluster evolution in general.

Numerous teams have found galaxy overdensities (ODs) around distant active galactic nuclei (AGN) and RGs, e.g., Best (2000); Best et al. (2003); Pentericci et al. (2000); Venemans et al. (2007); Haas et al. (2009); Falder et al. (2010, 2011); Galametz et al. (2012); Wylezalek et al. (2013); Hatch et al. (2014); Kotyla et al. (2016); Ghaffari et al. (2017). A similar strategy, using sub-millimeter galaxies as distant mass beacons, has found proto-clusters up to $z \sim 5$ (Steidel et al. 1998; Capak et al. 2011; Cai et al. 2017; Martinache et al. 2018; Miller et al. 2018, 2020). The studies using RGs as mass beacons revealed that galaxy ODs are found around about 50% of the RGs. Some RGs appear to be surrounded by fairly evolved clusters while others are not. The cases of no OD detection may indicate that the clustering of galaxies is still ongoing, and the concentration is not sufficiently high, pointing to the need to explore the clustering evolution further. This is a main topic of the current paper.

The brightest low-frequency-selected sample of RGs and quasars is that from the third Cambridge catalog (3C), selected at 178 MHz. It is known in two versions: a smaller one complete down to 10 Jy (Laing et al. 1983) and a larger one, which is used here, complete down to about 7.5 Jy; it contains 64 radio galaxies and quasars at $1 < z < 2.5$ (Spinrad et al. 1985). We here do not distinguish between RGs and quasars because of the orientation-based unified scheme of radio-loud AGN (Barthel 1989; Leipski et al. 2010; Wilkes et al. 2013). Recently two dedicated high- z 3C environment studies have been performed, one with *HST* and one with *Spitzer* observations:

Hilbert et al. (2016) presented *HST* imaging of a random sample of 22 high- z 3C sources in the visible (F606W) and near-infrared (F140W) as part of the snapshot program GO13023 (PI M. Chiaberge). In the description of the images, they noted the presence of numerous faint red galaxies surrounding the 3C sources. Subsequently Kotyla et al. (2016) studied the cluster environment of 21 fields. (3C 418 lies close to the galactic plane and is overcrowded by stars.) Cluster candidates were determined by two different approaches. Firstly, within a $40''$ radius of the 3C targets, the early-type galaxies (ETGs) were identified in every field by modeling each source with a Sérsic profile.

Then, using a simple passive evolution model, the expected location of the ETGs was derived on the red sequence (RS) in the color–magnitude diagram for each of the fields. For seven fields, the model coincides with the position of at least half of the ETGs. The complementary second approach involved a search for ODs and compared the object densities of the sample as a whole and individually against control fields taken from the GOODS-S region of the 3D-HST survey. With this method the fields of ten targets are cluster candidates. Four cluster candidates were found by both methods. The two methods disagree in some cases, depending on the specific properties of each field. Despite the success of finding clusters, the first approach may be limited by uncertainties in the Sérsic profile of faint sources. The second approach considers all galaxies irrespective of red and blue types; as shown below in this work, potential ODs may cancel out when red and blue galaxies exhibit an opposite OD behaviour.

The complete high-redshift 3C sample has been mapped with IRAC at the *Spitzer Space Telescope* albeit with moderate sensitivity (5σ detection limit of 22.4 mag at $4.5\mu\text{m}$). Using these IRAC data in combination with optical photometry (mostly upper limits) from Pan-STARRS, Ghaffari et al. (2017) searched for galaxy ODs. They selected candidate cluster member galaxies by color and magnitude cuts. Half of the 3C radio sources show ODs $> 3\sigma$ within $30''$ (~ 250 kpc) projected distance from the radio source compared to the surrounding galaxy densities measured in the $50''$ – $120''$ annulus. The ODs disappear for color cuts which are expected to remove ellipticals, suggesting that the $4.5\mu\text{m}$ -detected cluster candidates are mainly passive. As a special feature in that work, the ODs were presented and visualised with cumulative diagrams. In these diagrams the sorting of the 3C sources along increasing redshift provides an efficient way to read mean quantities from the cumulative slopes and to recognise redshift dependent evolutionary trends. The ODs show up below $z = 1.5$ but disappear beyond that redshift, suggesting either that the ODs do not exist — an interesting evolutionary effect — or that the ODs are not seen because the IRAC images are too shallow.

The IRAC cluster study revealed that the ODs should be measurable with a FoV $\sim 2'$ such as provided by the *HST* images (Hilbert et al. 2016). This led us to perform a new high- z 3C environment analysis based on the radial density profiles within the *HST* images. In comparison to the Kotyla et al. study, we consider fainter galaxies and make different use of galaxy colors and magnitudes. This paper is organised as follows: Section 2 lists the observations and data. Section 3 presents the resulting color magnitude diagrams, surface density maps and radial profiles, the central over- or under-density, brightness dependence of the overdensity, and the cumulative overdensity diagrams which allow for a quick statistical overview and recognition of redshift effects. Section 4 discusses the results and ends with the conclusions.

Throughout this work we adopt a standard Λ CDM cosmology with $H_0 = 70 \text{ km s}^{-1} \text{ Mpc}^{-1}$, $\Omega_\Lambda = 0.73$, and $\Omega_m = 0.27$ (Spergel et al. 2007). For the adopted cosmology, in the entire redshift range at $1 < z < 2.5$ a projected angular distance of $30''$ corresponds within 3 percent to 250 kpc. All magnitudes are AB, where zero mag corresponds to 3631 Jy.

2. Images, source catalogs and photometry

From the entire 3C catalog of 64 radio galaxies and quasars at $1 < z < 2.5$, a random subsample of 22 fields was mapped with the *HST* using WFC3 as part of the snapshot program GO13023 in the filters F606W and F140W. Hilbert et al. (2016) described

Table 1. The sample.

Name	RA (J2000)	Dec (J2000)	Redshift	Type ¹
3C 068.1	02 32 28.942	+34 23 46.810	1.238	Q
3C 186	07 44 17.539	+37 53 17.387	1.067	Q
3C 208.0	08 53 08.601	+13 52 54.790	1.110	Q
3C 210	08 58 10.047	+27 50 52.955	1.169	G
3C 220.2	09 30 33.557	+36 01 24.431	1.158	Q
3C 230	09 51 58.894	-00 01 27.206	1.487	G
3C 255	11 19 25.278	-03 02 50.554	1.355	Q
3C 257	11 23 09.474	+05 30 17.986	2.474	G
3C 268.4	12 09 13.661	+43 39 20.732	1.398	Q
3C 270.1	12 20 33.951	+33 43 11.503	1.532	Q
3C 287	13 30 37.708	+25 09 10.987	1.055	Q
3C 297	14 17 24.098	-04 00 48.834	1.406	G
3C 298	14 19 08.190	+06 28 34.806	1.437	Q
3C 300.1	14 28 31.274	-01 24 07.546	1.159	G
3C 305.1	14 47 09.393	+76 56 20.778	1.132	G
3C 322	15 35 01.332	+55 36 53.039	1.681	G
3C 324	15 49 48.793	+21 25 37.326	1.206	G
3C 326.1	15 56 10.168	+20 04 21.079	1.825	G
3C 356	17 24 19.023	+50 57 40.824	1.079	G
3C 432	21 22 46.277	+17 04 37.718	1.785	Q
3C 454.1	22 50 32.914	+71 29 18.312	1.841	G

¹ Type denotes quasar (Q) or radio galaxy (G), depending on whether or not broad emission lines have been identified in their spectra.

the data and the analysis of the 3C sources themselves. The F140W image size is $123'' \times 136''$, slightly smaller than that of F606W. Accounting for a small border ($5''$), the useful joint area is 4.3 square arcmin. The pixel size is $0''.0396$ (F606W) and $0''.128$ (F140W). We excluded 3C 418 from the sample, because it lies close to the Galactic plane ($b = 6^\circ$), and the images are crowded by stars. This leaves us with a sample of 21 HzRGs listed in Table 1.¹

Based on the *HST* images, Kotyla et al. (2016) created a source catalog. In brief, after parameter tuning, the SExtractor (SE) tool (Bertin & Arnouts 1996) was applied in the MAG BEST mode to the F140W images, obtaining a primary catalog with Kron photometry. Because the galaxies in the F606W images are more likely to be irregularly shaped, aperture photometry was used to measure the flux of all the components located within the region covered by the galaxy in the IR image. The photometric calibration to AB mag used F606W zero point 26.0691, F140W zero point 26.4524. All source photometry has been corrected for foreground Galactic extinction using the values from Schlafly & Finkbeiner (2011). Sources classified by SE to have stellar brightness profiles were flagged and excluded as well.

The aim of Kotyla et al. to precisely detect red sequences required high photometric quality and a two-filter detection. This led Kotyla et al. to exclude many faint, red sources. In contrast, for the study here we do not employ galaxy morphology; color uncertainties are less critical. Therefore, we used a deeper source catalog, created with the SE tool in the same manner as described above and in detail by Kotyla et al. (2016). The catalog used for the study here consists of two sub-catalogs, one detected in both filters (6371 sources) and one in IR only (2484 sources). The catalog contains about 450 galaxies per 3C field.

We derived the detection and completeness limits from $\log(N) - \log(S)$ diagrams (Fig. 1). The detection limits, i.e., the magnitude at which 98% of the sources are brighter, are 25.8 mag in F140W and 26.8 mag in F606W. The completeness limits ($\sim 90\%$) are about 1.3 mag brighter.

¹ Images are available on <https://hz3c.stsci.edu/Observations.html>

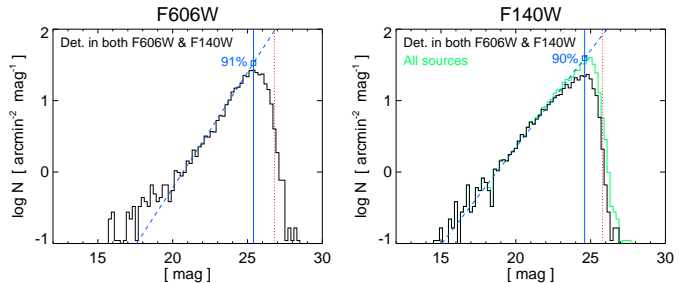


Fig. 1. Number counts around all 3C sources in the filters $0.606\text{ }\mu\text{m}$ and $1.4\text{ }\mu\text{m}$. Detections in both filters are shown in black, and the additional detections at $1.4\text{ }\mu\text{m}$ only are shown in green. The detection limit (red dotted line) is the magnitude at which 98% of the sources are brighter. The blue dashed line shows a linear fit. The completeness limit (blue solid line) and the completeness fractions are estimated relative to the extrapolation of the linear fit (blue square).

3. Results

3.1. Color-magnitude diagrams

Fig. 2 shows the color magnitude diagrams (CMDs) for each 3C field. Throughout this work we use the F606W – F140W color, henceforth denoted as opt–IR color or simply color, if not otherwise stated. Sources brighter than $F140W = 20$ mag have been excluded. The 3C radio galaxies lie around $F140W = 19.4 - 22.2$ mag, quasars are about 3 mag brighter (Hilbert et al. 2016). The radio galaxies have colors around 2–3 mag, suggesting that the searched-for red galaxy population also lies in this color range.

In order to determine the color threshold between passive (red) and star-forming (blue) galaxies, we consider two criteria. At $z \sim 1$, the F606W – F140W color corresponds to about rest frame $u - r$. These filters embrace the 4000 \AA break and thus measure the strength of this spectral feature. Based on Sloan Digital Sky Survey (SDSS) data of about 500 galaxies at $z < 0.4$, Stratéva et al. (2001) found that $u - r = 2.22$ separates passive and star-forming galaxies, as expected from their different stellar populations. Secondly, we have cross matched the two-filter-detected *HST* sample with the *Spitzer*/IRAC 3C sample of Ghaffari et al. (2017). For (the limited number of) unique matches, the supposed red sources at $z > 1$ with $F140W - [3.6] > 1$ show an average color $F606W - F140W = 2.8 \pm 0.8$. (For comparison: for $F140W - [3.6] > 0$, $F606W - F140W = 2.5 \pm 1.0$). These two considerations (from SDSS and *Spitzer*) suggest that a color threshold (ct , F606W – F140W) around $1.5 < ct < 2.22$ is well suited to separate passive and star-forming galaxies. To be independent of assumptions, we applied several color thresholds from 1.0 to 2.5 to see what the outcome is. In Fig. 2 we have used $ct = 1.5$ to separate red and blue galaxies for the catalog detected in both filters.

The color of the IR-only-detected sources is unknown but can be constrained as follows. The IR-only-detected sources must be fainter than the F606W completeness limit and therefore should lie above the completeness limit line in Fig. 2. The IR-only-detected sample may contain red sources as well as blue sources at the faint end. Therefore, to give it a short name, we here call it the *green* sample.²

² Our IR-only-detected *green* sample covers a broad color range and should not be confused with the population of *green valley galaxies* which has a narrow confined UV-opt color (Martin et al. 2007; Salim 2014).

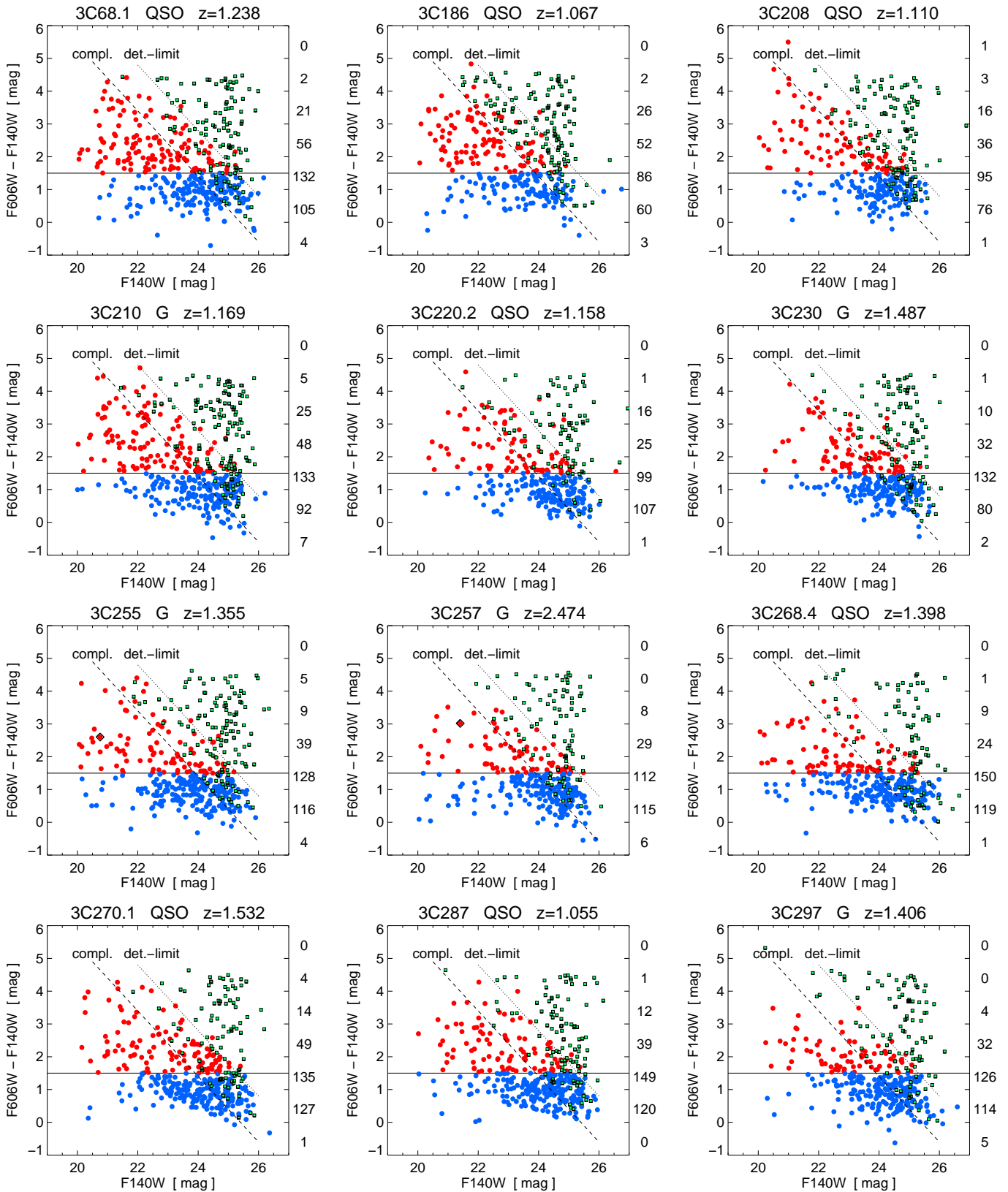
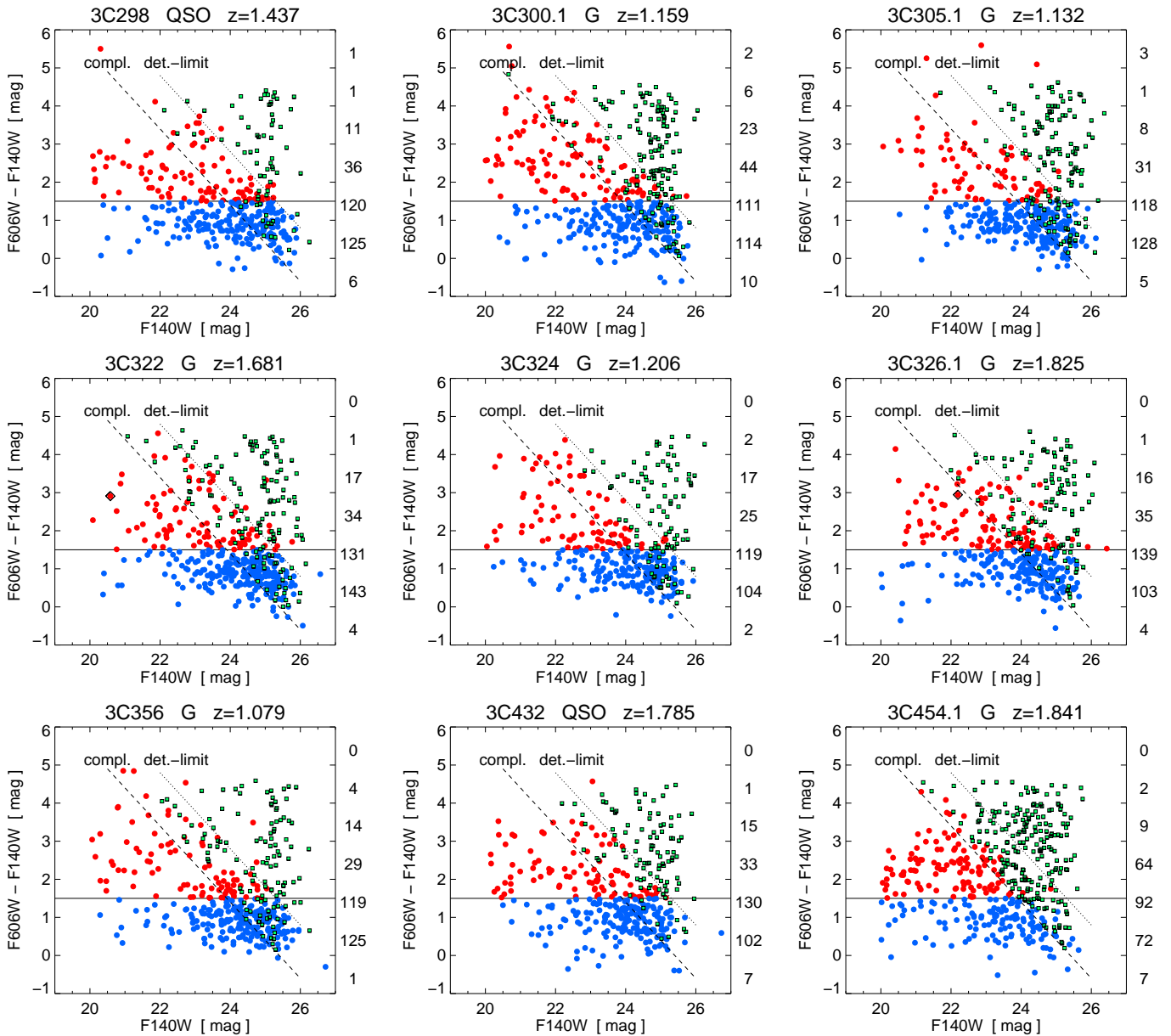


Fig. 2. Color-magnitude diagrams (CMDs) for the 3C fields. The plot titles list 3C name, type (Galaxy or Quasar) and redshift. The 3C source itself is marked in the CMD as a black diamond, if it fits into the plot range. Red and blue dots denote sources of the two-filter catalog, separated by the color threshold $ct = 1.5$ (solid horizontal line). The error bars of F140W are typically smaller than the size of the symbols and slightly exceed them at the faint end ($1\sigma < 0.3$ mag). However, in the color the error bars may be larger, reaching $1\sigma = 0.45$ mag, but we did not plot the error bars to avoid confusion. The green symbols mark the sources of the single filter sample, henceforth denoted the “green” sample, of which most sources are fainter than 24 mag. Their color is actually unknown and — for illustration only — the sources are here randomly placed above the completeness limits. The anti-diagonal dotted and dashed lines mark the color limits derived from the 3σ detection limits and the completeness limits. The numbers at the right Y-axis list the numbers of two-filter-detected sources in the respective color bins of width 1 mag.

**Fig. 2.** continued.

The *green* sample should have median color slightly redder than the two-filter detected sample. The median and average color of the two-filter detected sample at $23 < F140W < 25$ is 1.2 and 1.4 ± 0.8 , respectively. To estimate the median color of the *green* sample, we performed a stacking analysis: at all sky positions of an IR-only detected source, we stacked the IR and the optical images using a frame size of $10''$. We did this for several brightness bins ($23\text{--}24$, $24\text{--}25$, $25\text{--}26$ mag) and compared with stacking results of matching two-filter-detected subsamples. Visual inspection shows a clear median optical and IR stacked image, to which we applied the SE tool. The derived color of the median stacked images of the *green* sample is about 1.8, essentially independent of the brightness; this is about 0.5 mag redder than the median color of the two-filter-detected sample mentioned above. These estimates refer to the *median* colors and — at least for the two-filter-detected sample — the color distributions are broad and non-Gaussian with a tail

towards the red end (see the histogram numbers on the right Y-axis of Fig. 2).

The important realisation is that the *green* sample are simply faint(er) galaxies that were detected in the F140W images but not in F606W, and the stacking shows that they are, on average, redder than the two-filter-detected galaxies. The *green* sample reduces incompleteness bias which is introduced at the faint red end by the two-filter detected sample.

For the study here, we did not combine the *HST* 3C sample with the *Spitzer*/IRAC 3C sample for several reasons. Firstly, nearly 95% of the IRAC sources (in the *HST* field-of-view) are detected in F140W, so adding the IRAC sources would not increase the total number of sources. Secondly, the spatial resolution of *HST* is nearly ten-fold better than of IRAC, so up to 10% of the IRAC sources (in particular those with red F140W – [3.6] color) turn out to have double or multiple *HST* counterparts, and this prevents any secure photometric analysis for the most interesting (red) sources. Finally, the red sources can already be iden-

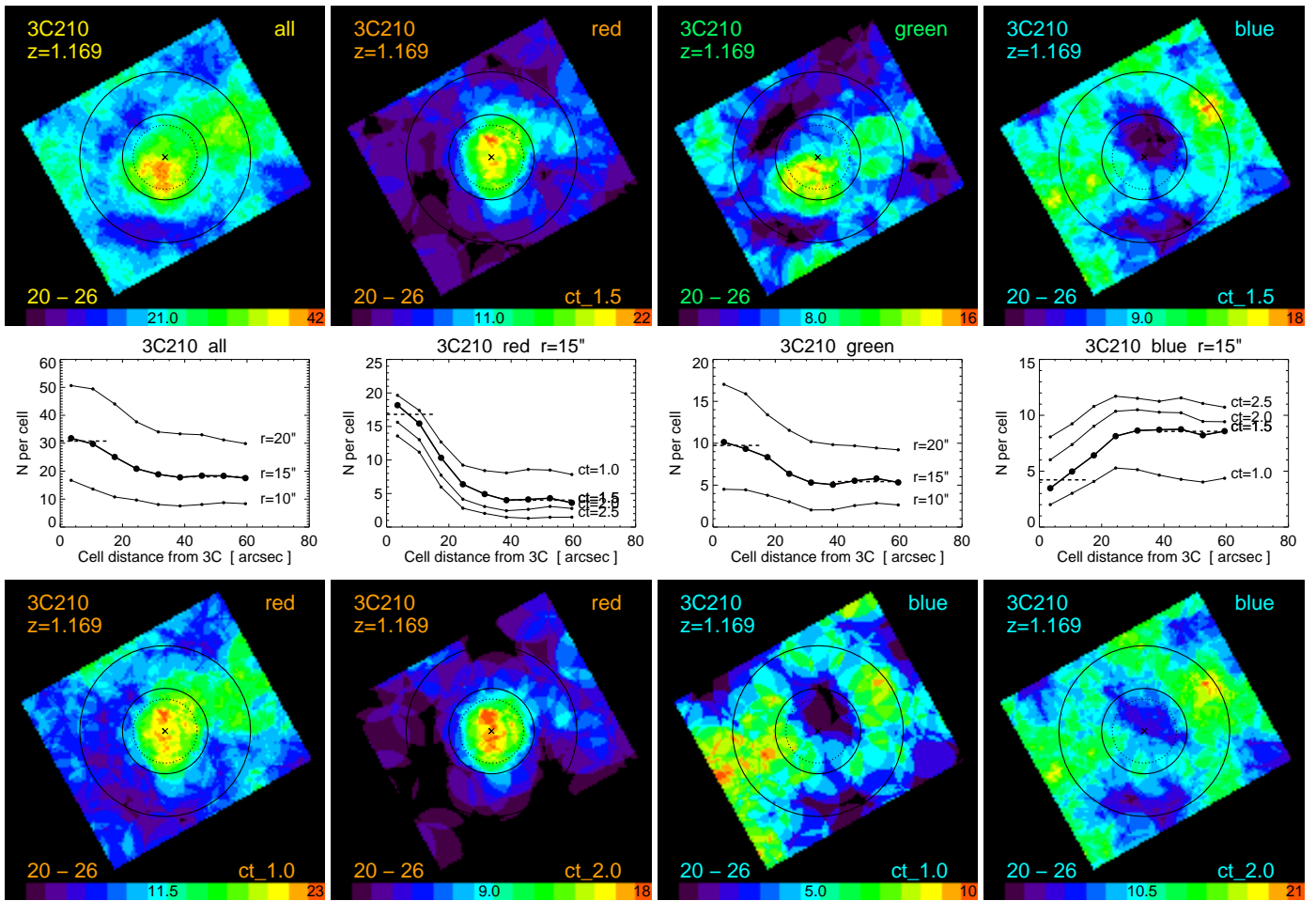


Fig. 3. Surface density maps and radial density profiles of the 3C 210 field. The top row shows the surface density maps for four selection criteria. These are from left to right: *all* galaxies, *red*, *green* and *blue* galaxies; for *red* and *blue* galaxies we used the color threshold $ct = 1.5$ as labeled in the bottom right corner. The magnitude range is $20 < F140W < 26$ as labeled in the bottom left corner. The map size is $2.5'$, North is up, East to the left. The black cross marks the position of the 3C source itself. The 3C source itself is used only as a signpost for a density enhancement and is therefore excluded from the density maps and all further density calculations. The dotted circle indicates the cell size ($r_c = 15''$), and the two solid circles mark a radius of $20''$ and $40''$ around the 3C source. The color bar at the bottom of the maps gives the linear range used for the map: from $N = 0$ (black, left end) to the maximal surface density per cell as labeled at the right end of the bar (red); light blue gives the numbers as labeled in the middle of the color bar. The bottom row shows the maps for *red* and *blue* galaxies, selected by color threshold $ct = 1.0$ and $ct = 2.0$. Corresponding to the maps in the top row, the middle row shows the mean radial surface density per cell, averaged in small bins of the distance d of the cell center from the 3C position. The radial bin size is $7''$; the first radial bin plotted at X-axis value $3.5''$ contains the average of the cells with $0'' \leq d < 7''$. The second radial bin plotted at X-axis value $10.5''$ contains the cells with $7'' \leq d < 14''$, and so on. The last radial bin is for $56'' \leq d < 63''$; then for a cell radius $r_c = 15''$ the outermost cells count galaxies up to a distance of $63'' + r_c = 78''$, i.e. at the corners inside the original image. The radial surface density is plotted for several samples: For the samples *all* and *green*, the results of three different cell sizes are shown. The thick line with fat dots marks the curve for cell radius $r_c = 15''$, which was used for the maps shown. The two other curves are for $r_c = 10''$ and $r_c = 20''$, without area normalisation, to avoid confusion of the three curves. For the samples *red* and *blue*, the results of four different color thresholds ct are depicted, each for cell size $r_c = 15''$. The thick line with fat dots marks $ct = 1.5$, which was used for the maps shown. The two horizontal long-dashed lines mark the average surface density of the center (SDC) and the periphery (SDP).

tified quite well in the *HST* data; simultaneously the *HST* data allow for exploring the blue galaxy population too. Therefore, we here use only the *HST* galaxy catalog. For the analysis the catalog is split into four samples named *red*, *blue*, *green* and *all*; *all* is the full catalog, *green* contains the F140W-only-detected galaxies, and *red* and *blue* galaxies are separated by ct , whereby we use as standard $ct = 1.5$ and note the ct value, if different from standard.

3.2. Surface density: maps and radial profiles

Using the two-filter-detected and the *green* galaxy catalogs, we have calculated surface density maps for each 3C field. For a

given parameter space (magnitude and color cut), we counted the galaxies within circular cells of radius $r_c = 15''$. The cells were centered on a 150×150 grid of $1''$ spacing. The surface density maps are oriented North-South / East-West and sufficiently large to cover the *HST* images (which are randomly oriented). Cells were masked out if they are not completely inside the *HST* image. Compared to the original image size, the size of the surface density map is slightly smaller (by twice the cell radius). For comparison, maps with $r_c = 10''$ and $r_c = 20''$ were also analysed.

Fig. 3 shows surface density maps and radial density profiles for the 3C 210 field. It is typical for fields with a clear central OD

(COD).³ Surface density maps and radial density profiles of the remaining sample are shown in the Appendix (Figs. A.1 to A.7). Visual inspection of the maps leaves no doubt that 3C 210 lies in the center of an overdensity of *red* galaxies with a radial extent of about 15''–30''. Outside of $r = 30''$, essentially no *red* galaxies are found. In contrast, the *blue* galaxies avoid the central $r = 20''$ area and are found in a few clumps at $r > 20''$. The maps using $ct = 1.0$ and $ct = 2.0$ corroborate the results for $ct = 1.5$. The *green* galaxies show a clear density enhancement with a peak slightly shifted to the south of 3C 210 but still within $r = 30''$ around 3C 210. The *green* population is about 24–26 mag and may include both *blue* and *red* galaxies (Fig. 2). One may speculate that the *green* density enhancement near 3C 210 is mainly built up of faint *red* galaxies. The OD near 3C 210 shows up when using *all* galaxies without any color constraints (the left map of the top row). We have also made maps with cell radius $r = 10''$ and $r = 20''$; they are of sharper and shallower contrasts respectively but similar to the $r = 15''$ maps.

We parameterized the density enhancements using radial surface density profiles. The middle row of Fig. 3 shows the mean radial surface density per cell. The radial surface densities increase with increasing cell size simply because more galaxies are contained in the larger cells, but the radial profiles are qualitatively similar, independent of cell size. This documents that the choice of $r = 15''$ produces stable results, which do not depend significantly on the cell size.

With increasing ct the level of the radial surface density curves increases and decreases for the *blue* and *red* samples simply because the number of galaxies changes. However, the shape of the radial profiles remains similar across the ct range. This indicates that the choice of $ct = 1.5$ also produces stable results.

To quantify the central over- or under-density of galaxies around the 3C source, we calculated the surface density of the center (SDC) and the periphery (SDP). Inspection of the density maps and radial density profiles of the entire sample shows that the density structures are compact and well covered within a radius $r = 30''$ (~ 250 kpc). Therefore SDC and SDP were calculated as the average of the first two and last four data points, respectively. The outermost cells entering the SDC calculation reach to $r = 14 + 15 = 29''$, and the innermost cells entering the SDP calculation reach $r = 42 - 15 = 27''$, but the overlap is negligible. From this we obtained the central overdensity as COD = SDC – SDP. A negative COD means under-density (UD). We consider the COD significance in Section 3.4.

The surface density maps and radial density profiles of the sample for $20 < F140W < 26$ are shown in Figs. A.1 to A.7. The radial density profiles are listed in Table D.1.

To summarize: the surface density maps reveal several density enhancements which, if not caused by fore- or background sources, indicate a clumpy structure of the forming galaxy clusters. The radial surface density profiles vary between the 3C sources. Both the maps and the profiles depend on the parameter space (magnitude and color cuts and slightly on the cell size). In some 3Cs the CODs are already evident in the “*all*” sample without any particular source selection, e.g., 3C 210, 3C 230, 3C 324. Most of these 3Cs show a strong COD of *red* sources, e.g., 3C 210, 3C 230 and 3C 324, while others do not, e.g., 3C 287 and 3C 298. Likewise, some 3Cs show a COD of both *red* and *blue* sources, e.g., 3C 230, while others reveal a clear lack of central *blue* sources which is just the opposite behaviour of the *red* sources, e.g., 3C 210 and 3C 324. For some 3Cs neither *red*

nor *blue* CODs are evident but only a COD of *green* (faint and presumably red) galaxies, e.g., 3C 68.1 and 3C 268.4.

3.3. Brightness dependence of the overdensity

Fig. 4 shows the CODs versus brightness of the four galaxy types *all*, *red*, *green* and *blue* for $ct = 1.5$. The 3C sources are sorted by increasing redshift (from bottom to top), in order to facilitate the recognition of redshift dependent trends. The brightness bins have a width of 1 mag. This leads to small numbers per brightness bin. A COD of $N = 5$ per square arcmin translates to 1 galaxy per cell of $r = 15''$, and for the purpose here we accept a COD as significant if it lies above this threshold. The figures reveal COD brightness trends which depend on the galaxy colors:

- 1) *Red* galaxies: at $z < 1.3$ most 3C sources show a striking COD of 20–24 mag *red* galaxies, e.g. 3C 356, 3C 208, 3C 210, 3C 324. At higher redshift (i.e., upper half of the panel) the COD weakens and shifts to fainter magnitudes (21 – 25 mag), e.g., 3C 297, 3C 230 at $z \sim 1.5$. The shift is consistent with the increase of the distance modulus $m - M$ by 1 – 2 mag with increasing redshift.⁴ This is reminiscent of a wave running through the parameter space, whereby the amplitude decreases with increasing redshift. Five 3C sources (3C 186, 3C 298, 3C 322, 3C 326.1, 3C 257) lack *red* COD in all brightness bins.
- 2) *Green* galaxies: nearly all 3C sources show a *green* COD in at least one magnitude bin, mostly at magnitude 23–26. Two 3C sources appear without *green* COD, 3C 255 and 3C 432. The *green* sample contains faint, presumably *red* galaxies, many of which are outside the completeness limit of the *red* sample (Fig. 2). Therefore the *green* CODs may be expected to be the continuation (or appearance) of the *red* CODs toward faint magnitudes. 3C sources lacking a *red* COD but showing a prominent *green* COD are 3C 186 and 3C 68.2 at $1.0 < z < 1.2$, likewise 3C 326.1 and 3C 454.1 at $z \sim 1.8$. For these two sources, the *green* COD is also supported by the surface density maps in Figs. B.7 and B.8.
- 3) *Blue* galaxies: they appear as CODs and UD (underdensities = negative CODs). The UD indicate a lack of *blue* galaxies in the center compared to the periphery. Most UD are found at low redshift $1 < z < 1.5$ (e.g., 3C 287, 3C 356, 3C 210). The *blue* UD, when found, are ~ 2 mag fainter than the *red* CODs (e.g., 3C 356, 3C 210), consistent with the expectation that the passive (giant) *red* cluster galaxies are brighter than the star-forming *blue* galaxies (even at rest frame optical wavelengths). The *blue* CODs, e.g., in 3C 208 and 3C 324, indicate the presence of *blue* starforming galaxies in the sky-projected central area; in physical space they could actually lie in the cluster periphery. A particular case is the *blue* COD in 3C 257 at $z = 2.5$, which we address further below (Sect. 3.4 and Fig. B.2). Sources with neither *blue* COD nor UD are 3C 220.2 and 3C 322.
- 4) *All* galaxies: along the entire brightness range, most 3C sources show a clear COD in at least two magnitude bins. For some 3C sources the CODs extend over three to four magnitudes, allowing for an estimate of the luminosity function (LF) of those sources contributing to the CODs. Examples with rising LF are 3C 220.2, 3C 268.4 and 3C 230; however, this is not the general case, and counter-examples with declining LF may be 3C 356, 3C 208 and 3C 210.

⁴ Example values for $m - M$ are: 44.20 at $z = 1.055$ (3C 287), 44.98 at $z = 1.406$ (3C 297), 45.62 at $z = 1.785$ (3C 432), and 46.49 at $z = 2.474$ (3C 257).

³ We distinguish between OD in general, for instance somewhere in the map, and central OD, which is OD around the 3C source.

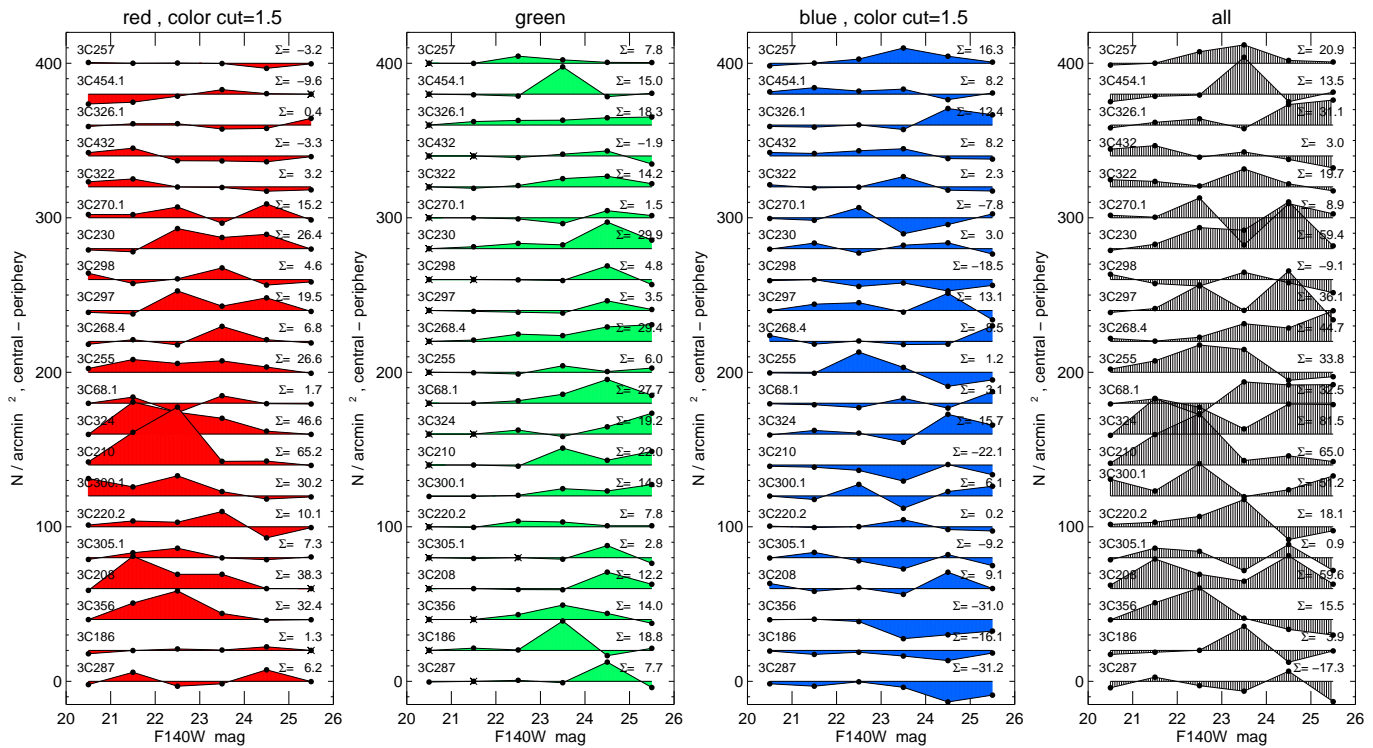


Fig. 4. Central overdensities (COD) versus brightness of the four sub-samples *red*, *green*, *blue* and *all*, for $ct = 1.5$. Each row shows the COD around the 3C as labeled on the left-hand side. The rows are subsequently shifted vertically by $20 / \text{arcmin}^2$. The 3Cs are sorted upwards by increasing redshift. For each 3C source, the total COD integrated over the brightness is labeled as Σ on the right-hand side. The 3C sources themselves have been excluded from the counts.

Fig. 4 treats *red* and *blue* galaxies using a fixed color cut $ct = 1.5$. To check how the choice of ct influences the *red* and *blue* brightness dependence, Fig. 5 shows COD versus brightness for *red* and *blue* galaxies going from $ct = 2.5$ (reddest cut) to $ct = 1.0$ (bluest cut). From that series, we continue with listing the main results:

- 5) COD of red sequence galaxies: for some 3C sources a clear *red* COD is present at $ct = 2.5$ which remains essentially unchanged when lowering the color threshold down to $ct = 1.0$. Likewise, in these sources the complementary *blue* UD shows the same behaviour. The five best examples are 3C 356, 3C 220.2, 3C 300.1, 3C 210, 3C 324, from bottom to top. This indicates that these 3C sources have assembled a red sequence (RS) composed of galaxies redder than $ct \sim 2.5$. For the brightness range of the RS we identify three types:
 - a) In two cases (3C 220.2, 3C 300.1) the *red* LF extends over 3–4 mag and increases slightly towards fainter galaxies, indicating that the RS has assembled already to low luminosities.
 - b) In two cases (3C 356, 3C 210) — both having the strongest CODs — the brightness range is narrow (21–23 mag), indicating the presence of relatively many luminous red giants but a lack of faint RS members.
 - c) In one case (3C 324) the *red* COD declines for increasing magnitude, indicating that the assembly of the RS towards the faint end is still ongoing.

Part of the missing >23 mag *red* galaxies may be contained in the *green* sample (Fig. 4), but (as shown in Sect. 3.5) its contribution is too small to lift the faint end of the *red* galaxy LF to a constant level as high as the bright peak.

- 6) COD with a fainter-for-bluer trend: the most prominent example of this type is 3C 230. For the reddest $ct = 2.5$, 3C 230 shows a *red* COD in the 22–23 mag bin; when continuously lowering the color cut allowing for bluer galaxies to enter the counts, the COD continuously grows: first at the 23–24 mag bin and then at 24–25 mag. Two other 3C sources with this fainter-when-bluer COD behaviour are 3C 255 and 3C 297. In addition, 3C 230 and 3C 297 possess a *green* COD at 24–25 mag. These findings together suggest that the RS has not yet evolved but is in the making with the faint *blue* galaxies already located in the (sky-projected) central area but having not yet reached the final red color.⁵

To summarise, comparing the *blue* and *red* CODs for a range of color thresholds allowed us to further constrain the presence and assembly of red sequences.

3.4. Significance and frequency of overdensities

In this Section, we consider how many 3C sources show a significant COD when using the standard parameters. We calculate the COD (= SDC – SDP) by two approaches, one using for each 3C its individual periphery and one using the average of all pe-

⁵ If the COD of *blue* faint galaxies is caused by a projection effect, such that in the 3-dimensional space these galaxies lie actually in front of or behind the center, and if this galaxy population is homogeneously distributed in the 3-dimensional peripheral annulus, then one may expect that the *blue* maps show this galaxy population in the periphery of our density maps. However, 3C 230 does not show any excess of *blue* galaxies in the periphery, in contrast to e.g., 3C 356 (see Figs. A.2 and A.7). This suggests that the COD of faint *blue* galaxies of 3C 230 is not due to sky-projection effects.

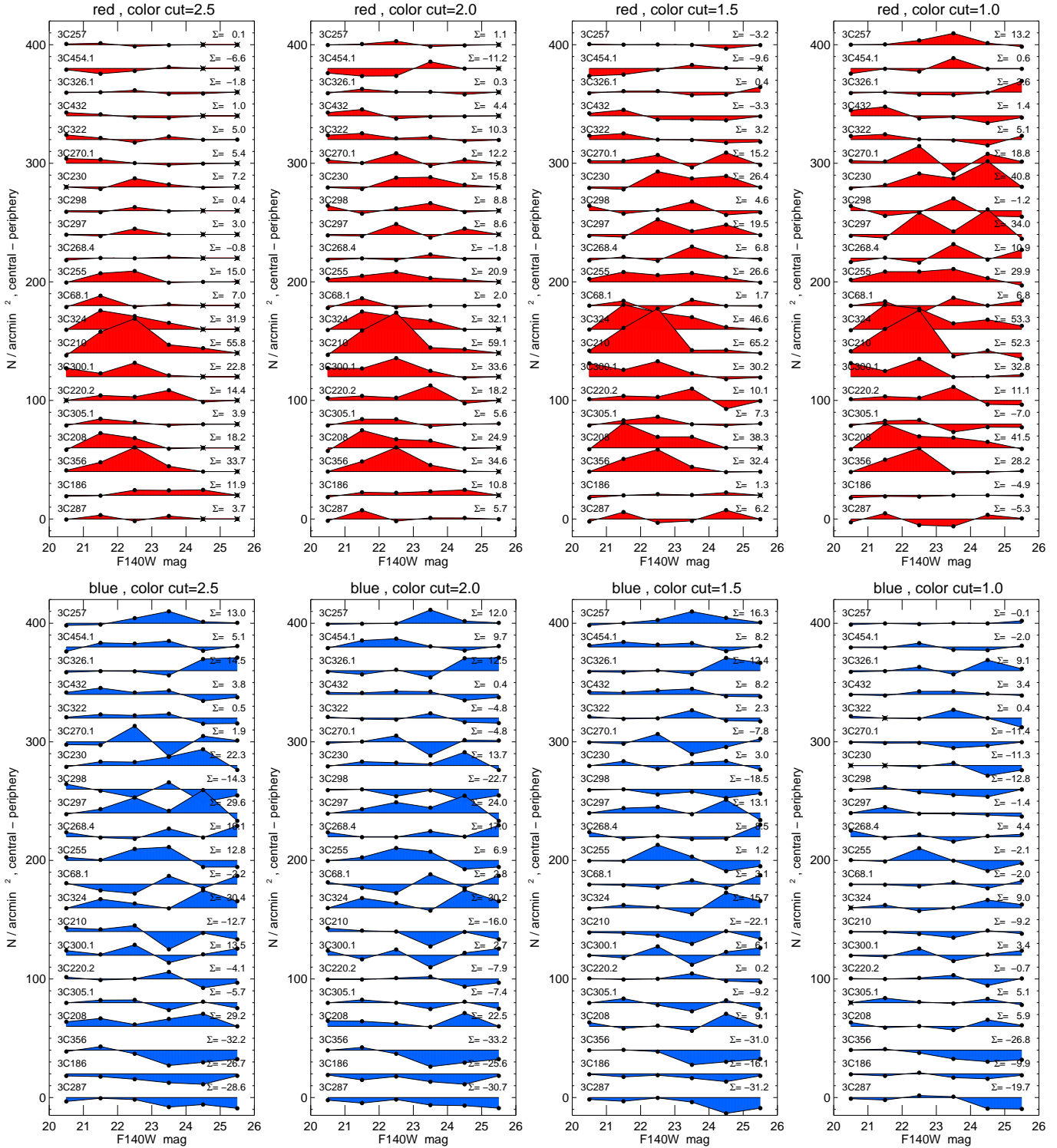


Fig. 5. Same as Fig. 4 but for red and blue sources and different color cuts $F606W - F140W = 1.0, 1.5, 2.0, 2.5$.

ipheries. Finally we compare with previous findings by Kotyla et al. (2016) and Ghaffari et al. (2017).

To estimate the significance of the COD, for our purpose it is relevant whether there is a local density enhancement centered on the 3C source, irrespective of the presence of other sub-clusterings in the map. Such clusterings in the periphery would increase σ_{SDP} . Fig. C.1 illustrates this for a few examples in Appendix C. Due to the fine cell grid spacing of $1''$, σ_{SDP} is determined quite accurately by a large number of cells (about 6 400).

In approach 1, we require that SDC is larger than the expectation value (EV) of SDP by three times the uncertainty of EV. unc_{EV} is the error of the mean, EoM: $\text{unc}_{\text{EV}} = \sigma_{\text{SDP}}/\sqrt{N}$. However, we have to take into account that SDP has been calculated from N cells which may overlap and thus are not independent. Therefore, we approximated the number of independent cells, N_{ic} , from the areas. $N_{\text{ic}} = A_p/A_c$ where A_p and A_{cell} are the area of periphery and cell, respectively. A_p is the area of the *HST* image (reduced by $15''$ for cell radius and $5''$

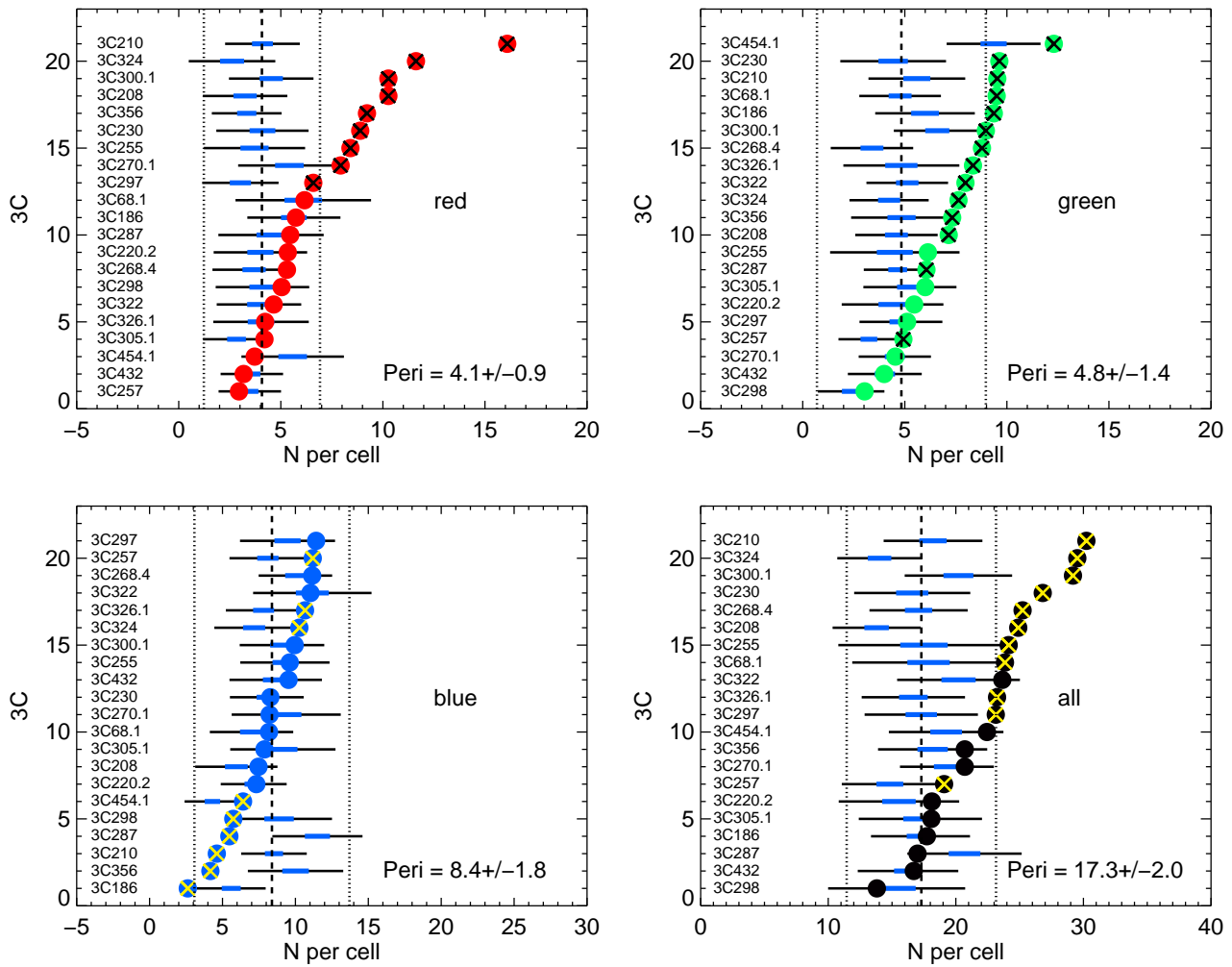


Fig. 6. Frequency of central overdensities, for the samples *red*, *green*, *blue* and *all*, for the brightness range $20 < \text{F140W} < 26$, cell radius $r_c = 15''$, $ct = 1.5$. In each panel, the 3Cs are sorted by the central surface density (Y-axis). For each 3C source, the X-axis shows the surface density of the center (SDC, fat dot) and of the periphery (SDP, horizontal bar with standard deviation as black bar and EoM as thicker blue bar) using values from Table D.2. The cross marks if the COD is significant (according to approach 1, see text). The vertical lines mark the average of the periphery calculated over all 3Cs (long-dashed) and the 3σ range (dotted); the corresponding values are labeled in the lower right corner.

for border) minus the central area of $r \sim 30''$. This leads to $N_{ic} \sim 13$ for $A_p = 103 \times 116 - \pi 30^2$ square arcsec and cell radius $r_c = 15''$. With this approach we consider a COD as significant if $\text{abs}(\text{OD}) > 3\sigma_{\text{SDP}}/\sqrt{N_{ic}}$.

Table D.2 lists the surface density of center and periphery, derived from the radial profiles, and the resulting COD classification, for each galaxy type (*blue*, *red*, *green*, *all*) and using as standard parameters the full brightness range ($20 < \text{F140W} < 26$) and a fixed $ct = 1.5$. Fig. 6 presents a graphic summary of the CODs, obtained by approach 1, together with SDC (fat dots) and SDP (horizontal bars).

Some 3C sources exhibit a significant COD without any doubt, as confirmed by inspection of the maps (e.g., Fig. 3). Others show no COD when using the standard parameters, in particular the full brightness range. Using a narrow brightness range or a ct different from 1.5, however, the radial profiles of some these sources indicate a weak COD (Figs. 4 and 5). Examples are 3C 68.1, 3C 257, 3C 270.1, 3C 322 3C 326.1, 3C 454.1. The narrow-brightness bins (Fig. 5) could suffer from low number statistics which could lead to randomly created CODs when applying the SDC–SDP calculation. Therefore we checked the corresponding maps as shown in Appendix B. The inspection

of the maps in the relevant parameter space shows that the 3C source in fact lies in a COD. In addition to the CODs derived using the standard parameters, Table D.2 lists these fine-tuned cases.

In total 16 out of the 21 observed 3C sources show a significant COD, i.e., lie in a clustering of *red/green* galaxies within a radius of 250 kpc centered on the 3C source. In about 10 of the 3C sources the *red/green* COD is accompanied by negative *blue* COD, which means that the *blue* galaxies avoid the center and/or are particularly located in the periphery (radius 250–500 kpc).

Approach 2 is illustrated by Fig. 6, where we consider the average of SDP over all 3C sources and the resulting 3σ range. The average is calculated using the individual SDP values from Table D.2. These SDP values are independent because drawn from different 3C sources. Therefore the overall SDP value derived from the periphery of all fields provides an independent estimate of the COD significance. According to approach 2, we consider a COD as significant if SDC lies outside the overall SDP 3σ range.

To summarise the comparison of approaches 1 and 2 from Fig. 6: for the *red* sample, both approaches yield a significant COD for nine and eight 3C sources respectively. A similar agree-

ment between the two approaches holds for the *all* sample. However, for the *green* and *blue* samples, approach 1 finds a larger number of significant CODs than approach 2 (green OD: 14 vs. 9, blue OD: 4 vs. 0, blue UD: 5 vs. 1). Approach 1 appears to be more sensitive in detecting CODs than approach 2. To understand this difference, we inspected the individual cases (maps and profiles) and find that approach 1 performs better to overcome the individual fluctuations of the SDP values (see e.g., the green OD of 3C 324 in Fig. A.6 and the blue UD of 3C 287 in Fig. A.4, both being of no doubt). To conclude, approach 2 yields more robust, conservative OD estimates but approach 1 is able to reveal more subtle *green* ODs and *blue* UDs which are well seen on the maps. In total, approach 1 yields 16 *red* and *green* CODs (9 *red* and additional 7 *green*). We here do not further refine the statistics, because the main results on the CODs are obtained from the *average* over 3C sub-samples as well as the *cumulative* overdensities below (next Section), for which the COD significance of an individual 3C source plays a minor role.

For comparison, Table D.2 lists also the RS and red OD findings in the previous *HST* study by Kotyla et al. (2016) (K16, their Table 3) and the OD findings in the *Spitzer/PanSTARRS* study by Ghaffari et al. (2017) (G17, their Table 5 col. 11). For K16, the RS detection required that at least 50% of the early-type galaxies match the position of the predicted red sequence, and the OD within a radius of 40'' was calculated against external control fields. For G17, the OD was calculated within 30'' compared to the periphery at 60''–120''. We discuss some typical cases:

- 3C 210 is a clear case with RS and red OD seen in both previous studies. Our surface density maps illuminate the strong galaxy concentration and corroborate the red (and green) COD. (In addition, the maps reveal the central lack of blue galaxies.)
- 3C 230 shows here a clear COD of *red* and *green* galaxies (for both approaches) which is corroborated by the surface density maps. However, K16 found only a marginal RS (at the discrimination border, 3/6 = 50% of the ETGs are on the predicted RS); both K16 and G17 failed to detect the OD which is closely below the 3σ criterion (74 vs. 77.7 for K16 and 7.64 vs. 7.85 for G17). A similar case is 3C 255 with a clear *red* COD (for both approaches), but only marginal RS in K16 and no OD in K16 and G17.
- 3C 356 shows here a clear COD of *red* galaxies (for both approaches) and a *blue* UD. Both OD and UD appear to cancel out resulting in a null OD for the *all* sample. This could explain why the OD does not show up in K16 (74 vs. 77.7). The detection of the RS marginally (5/12) failed in K16. The close environment of 3C 356 shows numerous faint red galaxies on the *HST* F140W image which are not detected on the *Spitzer/IRAC* image. If the IRAC image is too shallow, this could explain why the OD does not show up in G17 (8.91 vs. 10.86).
- 3C 186 shows here (only) a *green* COD consistent with the plenty of faint red sources seen on the images as reported by Hilbert et al. (2016). On the other hand, K16 found both a RS and an OD within 40'' radius suggesting that the RS should reflect in a *red* COD and the OD in an *all* COD here. However, the RS is marginal (at the discrimination border 4/8 = 50%). Also, the *red* SDP level is among the highest values consistent with the finding that 3C 186 has a rather extended (40'') red overdensity compared to the external comparison fields. We suggest that 3C 186 resides in a less organized overdensity of galaxies on larger scales, e.g., diffuse arrangements of multiple proto-clusters destined to merge

into a single massive cluster in the future (see Figs. A.1 and B.1). This picture is also consistent with the low concentration of the OD (radius 50'' rather than 30'') found in the *Spitzer/PanSTARRS* study by G17.

- 3C 220.2 shows a clear OD in the *Spitzer/PanSTARRS* study by G17 but lacks a significant OD in K16 (lowest OD of the sample) and here (both approaches). However, inspection of the surface density maps reveals several sub-clusterings and a faint OD centered on 3C 220.2 itself (Fig. A.2). Also, 3C 220.2 shows red sequence signatures in Figs. 4 and 5. We suggest that 3C 220.2 actually resides in an irregular overdensity of red galaxies, and that the unfavorable geometric constellation hindered our simple statistical approaches to realise the OD.

To summarise the comparison, each method (K16, G17 and here) has its specific advantages to detect overdensities and red sequences. With the exception of a few borderline cases, the previous RS/OD detections (K16, G17) are basically corroborated by the new analysis here, which in addition finds about 50% more CODs.

3.5. Cumulative overdensities

So far we have determined the COD for each 3C source in a given parameter space, e.g., *all*, *red*, *blue*, *green* and magnitude range and color threshold. For standard parameters the values are listed in Table D.1. In addition, a redshift dependent trend of the CODs is indicated in Figs. 4 and 5. In order to obtain a suited measure of the average CODs, we consider the cumulative distribution of CODs.⁶ Such cumulative diagrams enable us to recognise redshift trends because the X-axis of the cumulative diagrams, here the 3C sources, is sorted by increasing redshift. Thus, for the cumulative diagram CumCOD we sorted the 3C sources along redshift and then cumulate successively the measured individual CODs: CumCOD(i) = CumCOD(i-1) + COD(i), where COD(i) is the COD of the i^{th} 3C source. Also the slopes of the cumulative diagrams yield a quantitative measure for the average COD at a given redshift range together with the statistical significance. Steep/flat slopes indicate large/small COD and negative slopes a central UD.

Fig. 7 shows the CumCOD of the samples *all*, *red*, *green* and *blue* for $20 < F_{140W} < 26$. The main features of the CumCODs are:

- 1) *All*: a more or less steady increase with a mean slope $s \sim 6$ galaxies per cell per step. Irregularities (curvature at $X < 10$, $z < 1.2$) may be explained by negative *blue* CODs as we will see below.
- 2) *Red*: an almost linear increase with $s = 4$ galaxies per cell per step. The curvature seen in the *all* sample at $z < 1.2$ disappears. Depending on ct , the increase shows a tilt (or turn-over) towards a constant plateau. The turn-over is earliest for the largest $ct = 2.5$, about $X = 10$ ($z = 1.2$) and latest for $ct = 1.0$, about $X = 17$ ($z \sim 1.6$). The turn-over means that for higher redshift essentially no *red* CODs (at the given ct) are found. This could be a consequence of incompleteness of the *red* samples for detecting *red* CODs (completeness limit line in the CMDs in Fig. 2).
- 3) *Green*: an almost linear increase with $s = 2.5$ galaxies per cell per step without any discernible turn-over. This indicates

⁶ The method of cumulative CODs was also applied by Ghaffari et al. (2017) to the *Spitzer/PanSTARRS* study of the high- z 3C environment.

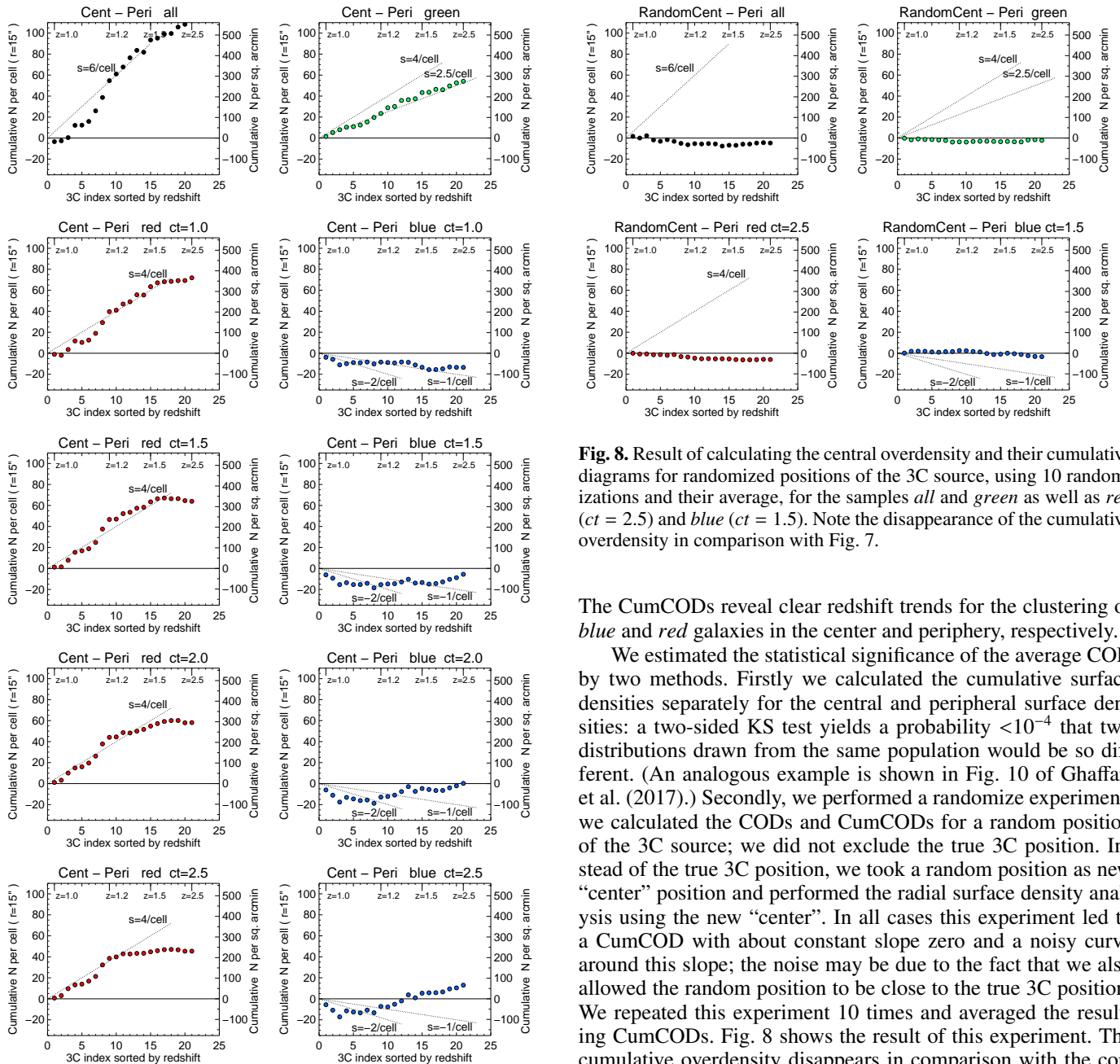


Fig. 7. Cumulative central overdensities of the samples *all*, *red*, *green* and *blue* for the brightness range $20 < F140W < 26$ and cell radius $r_c = 15''$, using several values of ct for the *red* and *blue* samples. The 3C sources are excluded from the counts. The X-axis is the index of the 3C source, sorted by redshift, as labeled at the top of each panel. To guide the eye, the diagonal dotted line marks a slope of an average central overdensity of s galaxies per cell per 3C field, s as labeled.

that the *green* sample is not as affected by incompleteness as the *red* sample.

- 4) *Blue*: for all ct the CumCODs decline at $z < 1.2$. This indicates a deficiency of *blue* galaxies in the center compared to the periphery. For $ct = 1.0$ this decline continues moderately to $z = 2.5$. For $ct > 1.0$, the CumCODs show a moderate upturn most evident at $ct = 2.5$ and for larger redshift ($z > 1.2$, $X = 10$). This upturn indicates that galaxies with color 1.0–2.5 contribute to the COD.

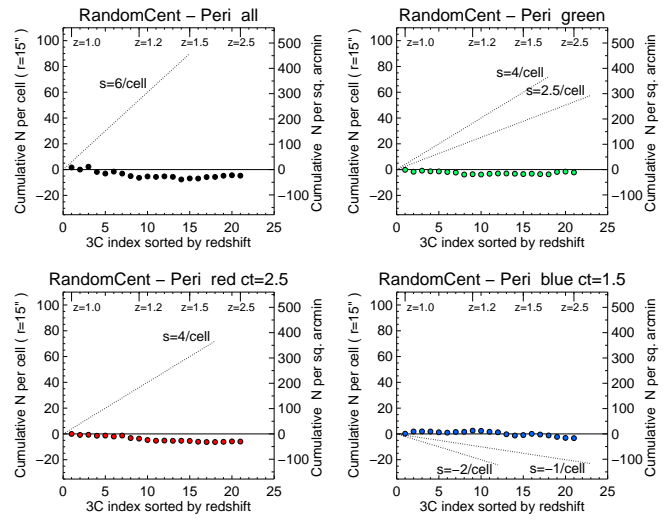


Fig. 8. Result of calculating the central overdensity and their cumulative diagrams for randomized positions of the 3C source, using 10 randomizations and their average, for the samples *all* and *green* as well as *red* ($ct = 2.5$) and *blue* ($ct = 1.5$). Note the disappearance of the cumulative overdensity in comparison with Fig. 7.

The CumCODs reveal clear redshift trends for the clustering of *blue* and *red* galaxies in the center and periphery, respectively.

We estimated the statistical significance of the average COD by two methods. Firstly we calculated the cumulative surface densities separately for the central and peripheral surface densities: a two-sided KS test yields a probability $<10^{-4}$ that two distributions drawn from the same population would be so different. (An analogous example is shown in Fig. 10 of Ghaffari et al. (2017).) Secondly, we performed a randomize experiment: we calculated the CODs and CumCODs for a random position of the 3C source; we did not exclude the true 3C position. Instead of the true 3C position, we took a random position as new “center” position and performed the radial surface density analysis using the new “center”. In all cases this experiment led to a CumCOD with about constant slope zero and a noisy curve around this slope; the noise may be due to the fact that we also allowed the random position to be close to the true 3C position. We repeated this experiment 10 times and averaged the resulting CumCODs. Fig. 8 shows the result of this experiment. The cumulative overdensity disappears in comparison with the corresponding panels in Fig. 7. The marginal negative slope for *all* and *red* suggests that for the randomized central positions the 3C source lies, on average, in the periphery slightly raising the SDP and lowering the random COD. The randomized results are similar for other parameters (*blue/red* galaxy samples). The two methods confirm that the CODs and CumCODs seen in Fig. 7 are significantly related to the 3C sources.

Fig. 9 shows the CumCOD for different brightness bins and the samples *all*, *red*, *green* and *blue*. The brightest bin shows no CODs. The main features of the CumCOD are, continuing the above numbering:

- 5) *All*: COD at all redshifts. At $z > 1.5$, galaxies with $23 < F140W < 24$ contribute most.
- 6) *Red*: COD of similar slope for 21–22 and 22–23 mag with turn-over at $z = 1.2$ and $z = 1.5$, respectively. For 23–24 mag, the slope becomes shallower, indicating fewer *red* galaxies in the center. For 24–25 and 25–26 mag essentially no *red* COD.

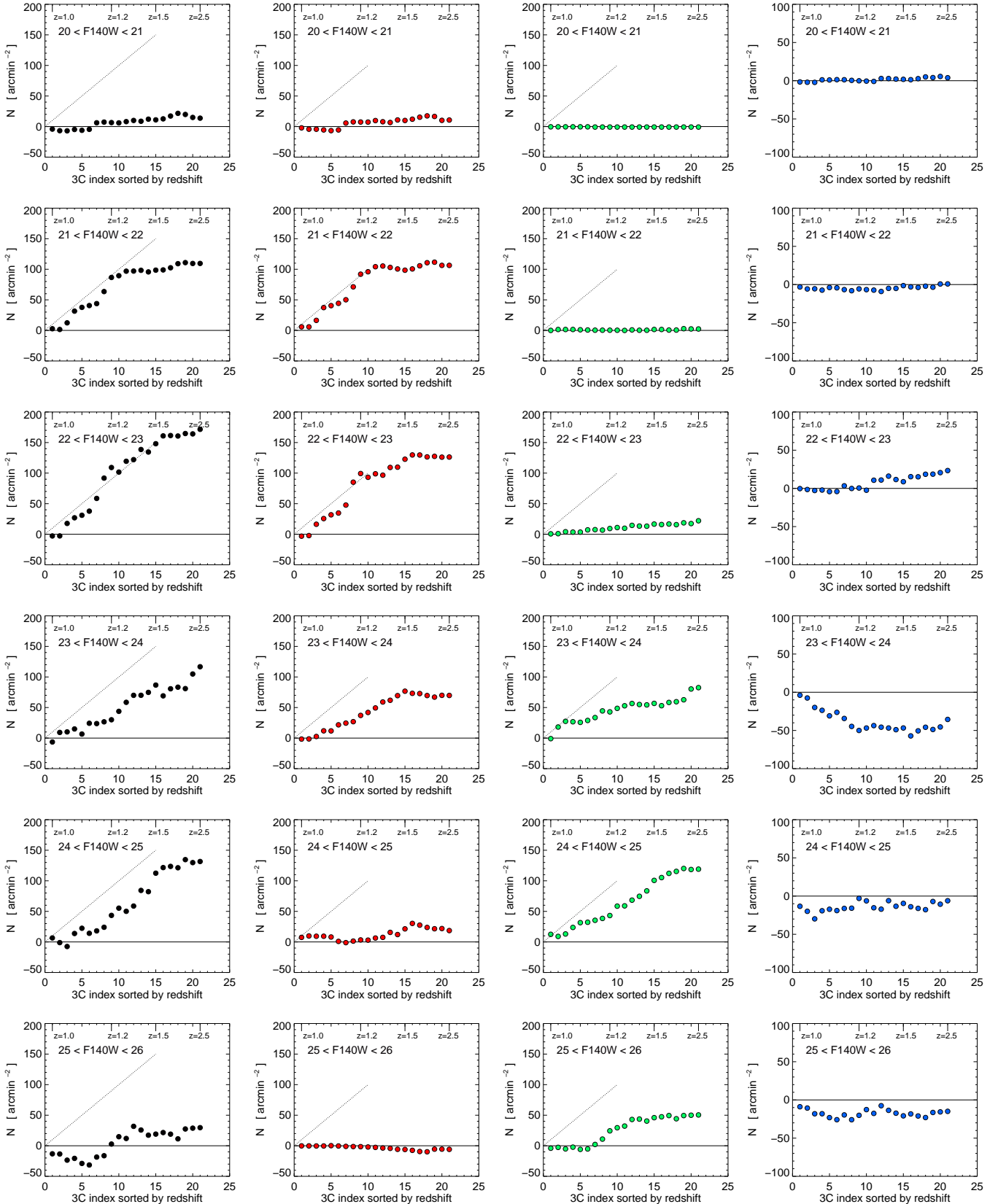


Fig. 9. Cumulative central overdensities for different brightness and the samples *all*, *red*, *green* and *blue* (from left to right); $ct = 1.5$ for the *red* and *blue* samples. The 3C sources are excluded from the counts. The X-axis is the index of the 3C source, sorted by redshift, as labeled at the top of each panel. The diagonal dotted line marks a slope of a cumulative central overdensity of $s = 10$ galaxies per square arcmin per 3C field. For the *blue* sample, the Y-axis is shifted and zoomed compared to the other three samples.

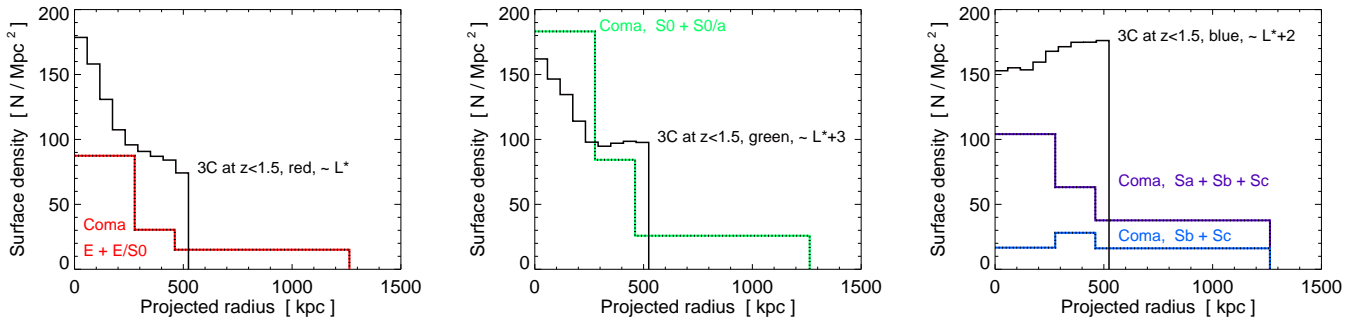


Fig. 10. Radial surface density profile of early and late-type galaxies in the Coma Cluster from Michard & Andreon (2008), and of *red/green/blue* galaxies in the 3C environment averaged over the 15 sources at $1 < z < 1.5$ with brightness range $20 < F140W < 26$ and $ct = 1.5$. The *red/green/blue* galaxies are shown in the left, middle and right panels, respectively. The background level at $r > 1300$ kpc has been subtracted for Coma but not for the 3Cs because the *HST* images do not extend so far out. For Coma the two cD galaxies are excluded from the counts, similar to excluding the 3C source itself from the 3C's radial surface density counts.

- 7) *Green*: Small COD for 22–23 mag, rather flat slope. The slope increases at 23–24 mag and further towards 24–25 mag. This indicates that the “missing” *red* CODs at 23–24 mag are compensated for by the *green* sample.
At 25–26 mag the CODs start at $X = 7$ ($z = 1.1$), indicating that *green* galaxies in this bin either do not contribute to the *red* COD or that their contributions to *red* COD and *blue* UD counter-balance each other. At $z < 1.4$, the slope of bin 25–26 is steepest, indicating that these galaxies may complete the missing faint *red* COD. At $z > 1.4$, the slope is rather flat, indicating that the faint *green* sources do not contribute or counter-balance as above.
- 8) *Blue*: Almost flat slope except for bin 23–24 at $z < 1.2$, where the decline indicates a deficiency of *blue* galaxies in the center compared to the periphery.

The analysis for the other ct between 1.0 and 2.5 confirms the picture which emerged from $ct = 1.5$.

3.6. Comparison with the Coma cluster

The Coma cluster is a paradigm local cluster. Coma has two cD galaxies, NGC 4874 (Coma A) and NGC 4889 (Coma B); both are radio-loud of the locally most frequent Fanaroff-Riley type FR-I, while most high- z 3C sources are of the FR-II type; that difference, however, is not expected to affect the comparison here.

Michard & Andreon (2008) have determined the morphology of galaxies of the Coma cluster and list them for three radial regions (their Figs. 1 and 4 and their Table 1). Using these data, excluding the dwarfs, we calculated the radial density profiles of Coma's luminous galaxies separated by type E + E/S0, S0 + S0/a and spiral galaxies. The profiles are depicted in Fig. 10. Overplotted are the average radial density profiles of the *red*, *green* and *blue* galaxies around the 3C sources at $z < 1.5$ (15 sources, with values taken from Table D.1 and converted to N/Mpc^2). The reason for choosing $z < 1.5$ is that the luminous *red* and faint *green* galaxies are well discernable in Fig. 9.

To compare the results of our color based galaxy types with these literature results which are based on morphological galaxy types, we have assumed that color and morphological classification are essentially equivalent, i.e., *red* and *blue* galaxies are early and late type galaxies, respectively. We note that dust-reddened star-forming galaxies may be miss-classified as passive, but dust reddening makes them dim; at rest frame UV-

optical wavelengths, a reddening by 1 mag corresponds to a dimming of about 2 mag. We suggest that most heavily dust-reddened star-forming galaxies are shifted below our detection limit.

The important results from Fig. 10 are: The average radial density profile of the *red* sample (i.e. the luminous *red* galaxies around the 3Cs) are roughly comparable to Coma's giant elliptical population E+E/S0. The *green* sample (presumably the less luminous *red* galaxies around the 3Cs) shows a lower central OD than Coma's S0+S0/a galaxies. And the *blue* sample shows a central lack of galaxies which may be comparable to Coma's Sb+Sc galaxies but differs when including Coma's Sa galaxies (Sa+Sb+Sc). We discuss these results in Sect. 4.5.

4. Discussion and Conclusion

4.1. Overdensity of *red* galaxies

We here assume that the *green* CODs are mainly built up of faint *red* galaxies. Therefore we consider both the *red* and *green* samples.

The strongest CODs, i.e., steepest CumCOD slopes, are found for bright *red* galaxies around $F140W = 22$ and at $z < 1.5$ (Fig. 9). Their luminosity is comparable to that of L^* galaxies at $1 < z < 1.5$, as Gabasch et al. (2004) have derived from their VLT/FORS deep field observations. The slope S of the CumCODs yields a mean COD of $s = 10$ (in units of galaxies per magnitude per square arcmin). The evolution of this steep slope can be followed towards fainter magnitudes and larger redshift, reminiscent of a wave running through the parameter space:

At magnitudes $23 < F140W < 24$, the slope decreases to $s = 5$, probably due to incompleteness of the faint *red* population. Strikingly this incompleteness appears to be compensated for by the *green* CumCOD slope of $s = 5$ (and we believe that this green compensation is in fact the case).

At $24 < F140W < 25$, the *red* CumCOD disappears, but the *green* CumCOD remains with a slope $s \sim 7$, which reaches to $z \sim 1.8$. Compared to $23 < F140W < 24$, the slope of the combined *red* and *green* CumCODs is slightly shallower.

At $25 < F140W < 26$, the *red* CumCOD is absent, but the *green* slope changes with redshift. It is flat at $z < 1.1$, then steep at $1.1 < z < 1.4$, and then flat again at $z > 1.4$. At $z < 1.1$, we interpret this as a lack of faint *red* COD; it appears that the mean luminosity function of the *red* galaxies declines at $L^* + 3$. The steep section of the *green* slope at $1.1 < z < 1.4$ could be the

continuation of the *green* COD seen in the 1 mag brighter bin. Finally, the flat slope at $z > 1.4$ indicates the lack of any *green* COD above that redshift; it indicates that the *green* COD seen at 1 mag brighter does not continue to larger redshift.

4.2. Central lack of blue galaxies

The surface density maps and radial density profiles demonstrate that at $z < 1.5$, the *blue* galaxies, on average, avoid the center (radius of $30'' = 250$ kpc around the 3C source). This is most prominent for 3C 210 and 3C 356 (Figs. 3 and A.7). It implies a spatial segregation of *red* and *blue* galaxies in the high- z 3C clusters.

This is the high- z analog of the Butcher-Oemler-effect: at intermediate redshift, clusters show a higher fraction of blue galaxies than in local clusters, and these are preferentially located in the periphery of the clusters (Butcher & Oemler 1978). This has been refined to become the density-morphology relationship: it is not the (projected) radial distance from the cluster center which determines the frequency of spirals, but rather the galaxy density (Dressler et al. 1997; Margoniner et al. 2001). Consensus on these effects is growing but still under discussion, e.g., see Andreon et al. (2006) and Andreon (2018).

4.3. Red sequences in the making

In the presentation of the *HST* images, Hilbert et al. (2016) already noted the presence of numerous red galaxies around the 3C sources well seen on F140W images but extremely dim at F606W. Kotyla et al. (2016) obtained a morphological classification of all galaxies and identified red-sequence, early-type galaxies, adopting galaxy evolution parameters with formation redshifts of 20 and 6.5, respectively. Because the morphological classification becomes uncertain for galaxies fainter than F140W ~ 24 mag, and in order to be free of assumptions about the galaxy evolution parameters, we here consider simply the *red* population, finding that for various color thresholds, on average, $ct = 1.5$ works well. The incompleteness of the *red* COD might be compensated for by the *green* COD.

We have estimated the average luminosity function (LF) of the RS galaxies, assuming that the combined *red* and *green* CODs capture the entire RS population within a radius of $30''$ (250 kpc) around the 3C source. For details we refer to Sect. 3.5, items 6+7, and Fig. 9. From these estimates, it turns out that the LF, on average, declines with decreasing brightness.

Our results for the high- z 3Cs are consistent with other findings:

Stott et al. (2007) explored the LF of ten massive X-ray-luminous clusters at $z = 0.5$ and found a deficit of faint red sequence galaxies compared to local clusters. They concluded that the faint red sequence (S0 population) builds up (quite late and slowly) between $z = 0.5$ and today. De Lucia et al. (2007) derived similar results between $z = 0.8$ and $z = 0.4$ from the ESO Distant Cluster Survey (EDisCS, 18 clusters).

Chan et al. (2019) explored the rest-frame *H*-band LF of red sequence galaxies in seven clusters at $1.0 < z < 1.3$ selected from the Gemini *z*-band “Rich Early Environments Survey”, combined with deep *Spitzer* observations (IRAC 5σ detection limit about 25 AB mag). By stacking the entire sample, they derived the LF across a range of 4–5 mag. They found a shallow faint end slope in contrast to the steeply rising slope in a sample of local clusters, suggesting that there is a deficiency of faint red sequence galaxies in clusters at high redshift.

On the other hand, in the galaxy cluster MS 1054–0321 at $z = 0.831$, Andreon (2006) found a fully evolved red sequence showing no deficit of faint red galaxies down to $M^* + 3.5$: the faint end of the color-magnitude relation is neither empty nor underpopulated compared to present-day and $z \sim 0.4$ LFs. Furthermore, in the study of the Coma cluster progenitor JKCS 041 at $z = 1.803$, Andreon et al. (2014) found a prominent red sequence down to stellar masses as low as $\log M/M_\odot = 9.8$ (about $M^* + 3.5$), which extends to a radius of 330 kpc around the cluster center. This extent is larger than the radius of 250 kpc used for deriving the OD of the 3Cs. Thus, if putative 3C clusters had a fully assembled RS, the faint end of the RS galaxies should lie in the periphery. Inspection of the surface density maps, however, does not support this possibility.

So far, for the RS of 3Cs we have considered average ODs. For some individual cases, e.g., 3C 220.2 and 3C 300.1, the RS may reach down to about $M^* + 3.5$ (Sect. 3.3 item 5a). Some other 3Cs, e.g., 3C 230, exhibit a rising LF for *red* galaxies using $ct = 1.0$ in Fig. 9, but for $ct \geq 1.5$, the faint end of these galaxies disappears step-by-step, revealing that they are present in the center but have intermediate or rather a *blue* color ($1.0 < \text{color} < 2.5$).

De Propris et al. (2015) carried out a joint photometric and structural analysis of red sequence galaxies in four clusters at a mean redshift $z = 1.25$ using optical and near-infrared *HST* imaging reaching at least three magnitudes fainter than M^* . Apart from the most massive galaxies, the high-redshift red-sequence galaxies are significantly more disk-dominated than their low-redshift analogues. These galaxies also show significant color gradients, not present in their low-redshift equivalents, most straightforwardly explained by radial age gradients. Our *HST* F606W snapshot images of the 3C sample are too shallow for detecting significant color gradients as those found in the deeper images of the De Propris et al.’s sample. Nevertheless, their results suggest that the galaxies with intermediate color surrounding the 3C sources are similar to the disk-like red population or their precursors seen by De Propris et al. (2015).

We conclude that the two cases (MS1054–0321 and JKCS 041) found by Andreon as well as 3C 220.2 and 3C 300.1 of our 3C study demonstrate that the RS may be fully assembled in some high- z clusters, but other studies indicate that this need not be the general case. For the majority of high- z clusters (or protoclusters), including clusters around a 3C source, the RS is still in the assembly phase. For the 3C sources a reservoir of *blue* galaxies which may transform/evolve to the RS is seen in the periphery and partly already in the center.

4.4. Redshift evolution

At $z < 1.5$, the *red* and *green* central overdensities are frequent (>80%, Table 3) and strong. The slopes of *red* and *green* CumCODs are $S = 4$ and $S = 2.5$ per cell, respectively. The coadded slope of $S = 6.5$ per cell corresponds to 32.5 galaxies per 3C source (Fig. 7). At $z > 1.5$, the central overdensity is less frequent and progressively composed of blue galaxies. The slope of *red* and *green* CumCOD reaches at most $S \sim 2.5$ per cell corresponding to 12.5 galaxies per 3C source. As shown by the density maps in Appendix B, the galaxies are less concentrated around the 3C sources (compared to $z < 1.5$). The sample contains only six 3C sources at $z > 1.5$. Compared to $z < 1.5$, the lower galaxy concentration and bluer colors of potential cluster member galaxies indicate that 3C clusters at $z > 1.5$ are in an earlier assembly phase.

4.5. Comparison with the Coma cluster

For the comparison, we make the assumption that a cluster or proto-cluster around a high- z 3C source is evolving to a Coma-like cluster today.

The *red* OD of the 3C sources is essentially made up of L^* galaxies (cf. Fig. 9). The *red* OD is comparable to the OD of Coma's luminous E+E/S0 population (left panel of Fig. 10). The surface density numbers are: $OD \approx 60/\text{Mpc}^2$ in Coma coming from $N1 = 90$ in the central bin up to radius 276 kpc, $N2 = 30$ in the second bin up to 461 kpc (see Table 1 of Michard & Andreon 2008). For the average of the 3C sources in the same radial bins as for Coma, we calculate a radius-weight average of $N1 = 120$ and $N2 = 90$, yielding $OD = 30/\text{Mpc}^2$, i.e., half of the OD for Coma. This refers to the average of the 3Cs, showing that their cluster centers have acquired already half of the giant red galaxies seen in todays Coma cluster.

Some 3C sources (e.g., 3C 210, 3C 230, 3C 356) have a *red* OD about a factor 2 stronger than the mean, possibly exceeding the OD of Coma E+E/S0 galaxies. These extreme 3C ODs are made up by a larger luminosity range extending to fainter galaxies. Then the extreme 3C ODs become comparable to the OD of Coma's E+E/S0 population (with part of the S0s added). We conclude that the luminous red cluster population is already well assembled in the high- z 3C environment. This adds support to the earlier interpretation by Dressler et al. (1997) from the study of intermediate-redshift clusters that “the formation of elliptical galaxies predates the formation of rich clusters and occurs instead in the loose-group phase or even earlier”.

The middle panel of Fig. 10 shows the *green* sources. The *green* OD of the 3Cs corresponds to a red population around L^*+2 . Comparison with Coma's OD of the S0+S0/a population shows that the *green* OD of the 3Cs is substantially lower, by about a factor 5. The numbers for Coma's radial bins are: For Coma, $OD \approx 100$ ($N1 = 185$, $N2 = 85$), and for 3C sources $OD \sim 20$ (radius-weight average of $N1 \sim 120$, $N2 \sim 100$). This supports the suggestion above (Sect. 4.3) that the S0 population has not yet fully evolved in the high- z 3C clusters (or proto-clusters).

The right panel of Fig. 10 shows the *blue* sources. The radial profile of Coma's spiral galaxies (Sa + Sb + Sc) increases towards the center; the increase is lower than for the early type galaxies (left and middle panel), a well known fact. In contrast to that increase, the radial profile of the 3C's *blue* galaxies declines from the periphery ($250 < r/\text{kpc} < 500$) towards the center. Sa galaxies are not really blue. Notably, the radial profile of Coma's Sb + Sc galaxies shows a small hump ($276 < r[\text{kpc}] < 461$) and a decrease towards the central radial bin, which is comparable to the decrease of 3C's *blue* galaxies. One may speculate that the radial profile of the 3C's *blue* galaxies decreases somewhere outside of $r > 500$ kpc, so that the periphery constitutes a hump similar to Coma's Sb + Sc galaxies.

The central lack of the 3C's *blue* galaxies suggests that they are cannibalised or have lost their gas while swirling from the field through an intra-cluster medium towards the cluster center, a well-known paradigm derived from local cluster observations by, e.g., Spitzer & Baade (1951). To quantify this effect, however, we need to know how the 3C's *blue* radial profile extends beyond 500 kpc to the field. The radial profile refers to the sky-projected surface density. If in 3-dimensional space the blue galaxies populate mainly a spherical shell of say ($250 < r[\text{kpc}] < 500$) and if the space density of the shell is enhanced compared to both center and field, then the projection effect may lead to a radial profile similar to what we observe for the 3Cs. We suggest

that this projection effect plays a role, and future observations with larger field-of-views are required to clarify this picture.

The comparison of *red*, *green* and *blue* galaxies with Coma leads us to conclude that the high- z 3C sources are not just becoming galaxy groups. Rather the foundation of a 3C galaxy cluster with luminous red cluster galaxies has largely been set, and (for most 3C sources) the formation of the red sequence is still ongoing from a reservoir of blue galaxies in the periphery.

4.6. Comparison with X-ray and Sunyaev-Zel'dovich

The complete high- z 3C sample of 64 sources has been observed at X-rays with *Chandra* and some with *XMM*. The observations in the *Chandra* Data Archive have been reinvestigated by Wilkes et al. (2013), Massaro et al. (2015), Stuardi et al. (2018), and Jimenez-Gallardo et al. (2020). The advantage of *Chandra* is its high spatial resolution, while *XMM* is more sensitive to faint extended emission provided that this emission is not outshone by bright embedded point sources. Essentially only 5 high- z 3C sources show extended X-ray emission potentially arising from a hot Intergalactic Medium (IGM). These sources are

- 3C 186 at $z \approx 1.07$ by *Chandra*. The diffuse X-ray emission from the cluster extends out to about 500 kpc radius (Siemiginowska et al. 2005, 2010). The compact steep spectrum (CSS) radio nature of 3C 186 hints at a major activity outburst within the past 10^7 years. Chiaberge et al. (2018) found a complex kinematics of BLR and NLR and indications consistent with a gravitational-wave-recoiling black hole, triggered by a merging binary black hole.
- 3C 210 at $z = 1.169$ by *Chandra*. Massaro et al. (2015) found both a hot core and extended emission in a region of $10''$ around the nucleus with an extent ratio parameter of 0.31. This is one of two or three high- z 3C sources with secure detection of extended, hot intra-cluster gas.
- 3C 298 at $z = 1.406$ by *XMM*, but Siemiginowska et al. (2008) note “pile-up”, making extended hot intra-cluster gas uncertain.
- 3C 294 at $z \approx 1.78$ by *Chandra*. Fabian et al. (2003) reported an hour-glass shaped extended emission with sharp edges. If the emission is of thermal origin, the gas is not in hydrostatic equilibrium. Based on ISAAC/VLT K_s -band images, Toft et al. (2003) reported a galaxy overdensity significant at the 2.4σ level (compared to the local field density) and concluded that, if the galaxies are in a cluster at $z = 1.786$, they must be dominated by young stellar populations with different star-formation histories. Based on LBT adaptive optics NIR imaging and optical spectroscopy, Heidt et al. (2019) reported inconclusive but potential evidence that 3C 294 hosts a binary black hole. If so, the anticipated exceptional feedback make the presence of a hot intra-cluster medium in hydrostatic equilibrium unlikely.
- 3C 322 at $z = 1.779$ by *XMM*. Belsole et al. (2004) noted “The poor statistics do not allow us to constrain well the origin of the X-ray emission.”

On the other hand, for the 3C sample at intermediate redshift ($0.45 < z < 1$), Belsole et al. (2007) reported that 19 out of 20 sources lie in a clustering of galaxies, and 60% of the 3C sources show clear signatures of an extended, evolved X-ray cluster. Lower sensitivity, in principle, could explain the lower X-ray detection rate of high- z 3C clusters. For the intermediate- z sample the exposure time was mostly between 10 and 50 ks (2 sources lower, 2 sources higher), but for the high- z 3C sample it

was typically between 12 and 40 ks (Massaro et al. 2015). It appears hard to explain by the small sensitivity difference and small distance difference, why all six of six 3C sources at $0.8 < z < 1.0$ have been detected (Belsole et al. 2007) and only two out of 20 at $1.0 < z < 1.2$ (Massaro et al. 2015). We conclude that, with a few exceptions, the high- z 3C sources are not yet embedded in an evolved X-ray cluster.

The Sunyaev-Zel'dovich effect (SZE) arises when the hot intra-cluster electrons Compton-upscatter cosmic microwave background (CMB) photons. To our knowledge, also supported by private communication with Dave Clements and Frank Bertoldi, the high- z 3C sample has not been searched for the SZE. Cavaliere et al. (2002) discussed the difference between galaxy groups and clusters with regard to measurable signatures of the inter-galactic medium. If the high- z 3C sources tend to assemble only groups (instead of clusters), then any inter-galactic medium may easily be expelled by AGN outflows. In any case, the expected SZE is small and may be affected by the imprint of the feedback of an active galactic nucleus onto the surrounding medium (Chatterjee & Kosowsky 2007). Lapi et al. (2003) computed how the SZE is enhanced by the transient blast wave driven by an active quasar and how it is depressed when the equilibrium is recovered with a depleted density. On the other hand, Soergel et al. (2017) combined microwave and sub-mm data from *Herschel/Planck* with all-sky far-infrared maps from the *AKARI* satellite to study the stacked SZE on Sloan Digital Sky Survey (SDSS) redMaPPer catalogue of galaxy clusters (median $z = 0.37$). They compared with the stacked SZ signal of ten thousand quasar hosts at median $z = 2.07$. They found a significant SZE and concluded that the mean imprint of quasar feedback is negligible. Because of the huge number of fields needed for a good S/N stacked image, the detection of an SZE signal of the high- z 3C sources/clusters will be challenging.

To conclude, the clustering of galaxies around high-redshift 3C sources appears to precede, with a few exceptions, the assembly of detectable mass concentrations and of extended hot X-ray gas found for most of the lower-redshift 3C sources.

4.7. Outlook

Surface density maps revealed the clustering of red and blue galaxies around a representative sample of 21 high- z 3C sources. Despite the limited field-of-view ($r \sim 500$ kpc), we found a spatial segregation of red and blue galaxies populating preferentially the central and outer regions of the anticipated clusters, respectively. We found also redshift trends, although our sample includes only 6 sources at $z > 1.5$. These findings make future studies with larger fields and larger samples promising, in particular to corroborate the redshift trends and to investigate possible sub-clustering. While the density maps and the randomised experiments of the central overdensities strongly support that the density enhancements are associated with the 3C sources, spectroscopic observations will verify cluster membership of the candidates and enable a kinematic study.

Acknowledgements. This work is based on observations taken by the HST-3C collaboration, program GO 13023, with the NASA/ESA HST, which is operated by the Association of Universities for Research in Astronomy, Inc., under NASA contract NAS 5-26555. The 3C environment research at Ruhr-University Bochum is supported by funds from Deutsche Forschungsgemeinschaft (DFG grant HA3555/13-1). We thank Dave Clements, Frank Bertoldi and Chiara Stuardi for suggestions.

References

- Aguado-Barahona, A., Barrena, R., Strebyanska, A., et al. 2019, A&A, 631, A148
- Andreon, S. 2006, MNRAS, 369, 969
- Andreon, S. 2018, A&A, 617, A53
- Andreon, S., Newman, A. B., Trinchieri, G., et al. 2014, A&A p, 565, A120
- Andreon, S., Quintana, H., Tajer, M., Galaz, G., & Surdej, J. 2006, MNRAS, 365, 915
- Barrena, R., Ferragamo, A., Rubiño-Martín, J. A., et al. 2020, A&A, 638, A146
- Barrena, R., Strebyanska, A., Ferragamo, A., et al. 2018, A&A p, 616, A42
- Barthel, P. D. 1989, ApJ, 336, 606
- Belsole, E., Worrall, D. M., Hardcastle, M. J., Birkinshaw, M., & Lawrence, C. R. 2004, MNRAS, 352, 924
- Belsole, E., Worrall, D. M., Hardcastle, M. J., & Croston, J. H. 2007, MNRAS, 381, 1109
- Bertin, E. & Arnouts, S. 1996, A&A ps, 117, 393
- Best, P. N. 2000, MNRAS, 317, 720
- Best, P. N., Lehnert, M. D., Miley, G. K., & Röttgering, H. J. A. 2003, MNRAS, 343, 1
- Bleem, L. E., Stalder, B., de Haan, T., et al. 2015, ApJS, 216, 27
- Butcher, H. & Oemler, A., J. 1978, ApJ, 226, 559
- Cai, Z., Fan, X., Bian, F., et al. 2017, ApJ, 839, 131
- Capak, P. L., Riechers, D., Scoville, N. Z., et al. 2011, Nature, 470, 233
- Carlstrom, J. E., Ade, P. A. R., Aird, K. A., et al. 2011, PASP, 123, 568
- Cavaliere, A., Lapi, A., & Menci, N. 2002, ApJ, 581, L1
- Chan, J. C. C., Wilson, G., Rudnick, G., et al. 2019, ApJ, 880, 119
- Chatterjee, S. & Kosowsky, A. 2007, ApJ, 661, L113
- Chiaberge, M., Gilli, R., Lotz, J. M., & Norman, C. 2015, ApJ, 806, 147
- Chiaberge, M., Tremblay, G. R., Capetti, A., & Norman, C. 2018, ApJ, 861, 56
- De Lucia, G., Poggianti, B. M., Aragón-Salamanca, A., et al. 2007, MNRAS, 374, 809
- De Propris, R., Bremer, M. N., & Phillipps, S. 2015, MNRAS, 450, 1268
- Dressler, A., Oemler, Augustus, J., Couch, W. J., et al. 1997, ApJ, 490, 577
- Eisenhardt, P. R., Stern, D., Brodwin, M., et al. 2004, ApJS, 154, 48
- Eisenhardt, P. R. M., Brodwin, M., Gonzalez, A. H., et al. 2008, ApJ, 684, 905
- Fabian, A. C., Sanders, J. S., Crawford, C. S., & Ettori, S. 2003, MNRAS, 341, 729
- Falder, J. T., Stevens, J. A., Jarvis, M. J., et al. 2011, ApJ, 735, 123
- Falder, J. T., Stevens, J. A., Jarvis, M. J., et al. 2010, MNRAS, 405, 347
- Fassbender, R., Böhringer, H., Nastasi, A., et al. 2011, New Journal of Physics, 13, 125014
- Gabasch, A., Bender, R., Seitz, S., et al. 2004, A&A, 421, 41
- Galametz, A., Stern, D., De Breuck, C., et al. 2012, ApJ, 749, 169
- Ghaffari, Z., Westhues, C., Haas, M., et al. 2017, Astronomische Nachrichten, 338, 823
- Gladders, M. D. & Yee, H. K. C. 2000, arXiv e-prints, astro
- Haas, M., Willner, S. P., Heymann, F., et al. 2009, ApJ, 695, 724
- Hatch, N. A., Wylezalek, D., Kurk, J. D., et al. 2014, MNRAS, 445, 280
- Heidt, J., Quirrenbach, A., Hoyer, N., et al. 2019, A&A, 628, A28
- Hennig, C., Mohr, J. J., Zenteno, A., et al. 2017, MNRAS, 467, 4015
- Hilbert, B., Chiaberge, M., Kotyla, J. P., et al. 2016, ApJS, 225, 12
- Hildebrandt, H., Muzzin, A., Erben, T., et al. 2011, ApJ, 733, L30
- Huang, N., Bleem, L. E., Stalder, B., et al. 2020, AJ, 159, 110
- Jimenez-Gallardo, A., Massaro, F., Prieto, M. A., et al. 2020, arXiv e-prints, arXiv:2007.02945
- Khullar, G., Bleem, L. E., Bayliss, M. B., et al. 2019, ApJ, 870, 7
- Kotyla, J. P., Chiaberge, M., Baum, S., et al. 2016, ApJ, 826, 46
- Laing, R. A., Riley, J. M., & Longair, M. S. 1983, MNRAS, 204, 151
- Lapi, A., Cavaliere, A., & De Zotti, G. 2003, ApJ, 597, L93
- Leipski, C., Haas, M., Willner, S. P., et al. 2010, ApJ, 717, 766
- Mantz, A. B., Abdulla, Z., Allen, S. W., et al. 2018, A&A p, 620, A2
- Margoniner, V. E., de Carvalho, R. R., Gal, R. R., & Djorgovski, S. G. 2001, ApJL, 548, L143
- Martin, D. C., Wyder, T. K., Schiminovich, D., et al. 2007, ApJS, 173, 342
- Martinache, C., Rettura, A., Dole, H., et al. 2018, A&A p, 620, A198
- Massaro, F., Harris, D. E., Liuzzo, E., et al. 2015, ApJS, 220, 5
- Mehrtens, N., Romer, A. K., Hilton, M., et al. 2012, MNRAS, 423, 1024
- Michard, R. & Andreon, S. 2008, A&A p, 490, 923
- Miley, G. & De Breuck, C. 2008, A&A pr, 15, 67
- Miller, T. B., Chapman, S. C., Aravena, M., et al. 2018, Nature, 556, 469
- Miller, T. B., Chapman, S. C., Hayward, C. C., et al. 2020, ApJ, 889, 98
- Muzzin, A., Wilson, G., Yee, H. K. C., et al. 2009, ApJ, 698, 1934
- Papovich, C., Momcheva, I., Willmer, C. N. A., et al. 2010, ApJ, 716, 1503
- Pentericci, L., Kurk, J. D., Röttgering, H. J. A., et al. 2000, A&A, 361, L25
- Salim, S. 2014, Serbian Astronomical Journal, 189, 1
- Schlafly, E. F. & Finkbeiner, D. P. 2011, ApJ, 737, 103
- Siemiginowska, A., Burke, D. J., Aldcroft, T. L., et al. 2010, ApJ, 722, 102
- Siemiginowska, A., Cheung, C. C., LaMassa, S., et al. 2005, ApJ, 632, 110
- Siemiginowska, A., LaMassa, S., Aldcroft, T. L., Bechtold, J., & Elvis, M. 2008, ApJ, 684, 811

- Soergel, B., Giannantonio, T., Efstathiou, G., Puchwein, E., & Sijacki, D. 2017,
MNRAS, 468, 577
Spergel, D. N., Bean, R., Doré, O., et al. 2007, ApJS, 170, 377
Spinrad, H., Marr, J., Aguilar, L., & Djorgovski, S. 1985, PSAP, 97, 932
Spitzer, Lyman, J. & Baade, W. 1951, ApJ, 113, 413
Steidel, C. C., Adelberger, K. L., Dickinson, M., et al. 1998, ApJ, 492, 428
Stott, J. P., Smail, I., Edge, A. C., et al. 2007, ApJ, 661, 95
Strateva, I., Ivezić, Ž., Knapp, G. R., et al. 2001, AJ, 122, 1861
Stuardi, C., Missaglia, V., Massaro, F., et al. 2018, ApJS, 235, 32
Toft, S., Pedersen, K., Ebeling, H., & Hjorth, J. 2003, MNRAS, 341, L55
Venemans, B. P., Röttgering, H. J. A., Miley, G. K., et al. 2007, A&A p, 461,
823
Wilkes, B. J., Kuraszkiewicz, J., Haas, M., et al. 2013, ApJ, 773, 15
Wilson, G., Muzzin, A., Yee, H. K. C., & SpARCS Collaboration. 2009, in American Astronomical Society Meeting Abstracts, Vol. 214, American Astronomical Society Meeting Abstracts #214, 300.02
Wylezalek, D., Galametz, A., Stern, D., et al. 2013, ApJ, 769, 79

Appendix A: Surface density: maps and radial profiles of the entire sample

Figs. A.1 to A.7 show the surface density maps and radial profiles of the entire sample. Explanations are given in Sect. 3.2.

Appendix B: Surface density maps of selected 3C sources

For some 3C sources, the COD is not revealed by the standard parameters (20–26 mag, $ct = 1.5$ and $r_c = 15''$). When tuning the parameters, in particular for the brightness range, CODs can appear (Figs. 4 and 5). Here we check whether these CODs are confirmed by the density maps when using the corresponding parameters.

- 3C 68.1 and 3C 186: The maps (Fig. B.1) confirm a clear OD of *green* galaxies at 23–25 mag, but neither *red* nor *blue* galaxies show an OD.
- 3C 257 at $z = 2.474$ has the highest redshift of our sample. The radial profile analysis indicates an OD for *all*, *red* ($ct = 1.0$), and *blue* ($ct = 2.5$) around 22–24 mag. The maps (Fig. B.2) confirm a clear COD of galaxies at 22–24 mag with a color between 1.0 and 2.5. This OD is consistent with the finding of star-forming early-type galaxies around 3C 257 by Kotyla et al. (2016).
- 3C 270.1: the maps (Fig. B.3) confirm a COD of moderately *red* ($ct = 1.0$) galaxies at 22–26 mag, which lies between two enhanced density structures at $r = 40''$. The *red* COD corresponds to a central deficiency of *blue* galaxies suggesting that some transformation from blue to red galaxies has taken place. Based on *Spitzer*/IRAC images, a *red* COD (using $r = 50''$) has been found by Haas et al. (2009) and confirmed by Galametz et al. (2012), consistent with the results from the surface density map here.
- 3C 287 and 3C 305.1: the maps (Fig. B.5) show a marginal clustering of *green* galaxies near 3C 287 and no evidence for *red* clustering associated with 3C 305.1.
- 3C 297: the maps (Fig. B.4) confirm a clear COD of moderately *red* ($ct = 1.0$) galaxies at 22–25 mag, already indicated by the radial SD analysis.
- 3C 322: this source at $z \sim 1.7$ lacks any prominent COD in the radial SD analysis. The maps with $r_c = 20''$ reveal that the source lies at the border of a *green* COD extending towards the southwest (Fig. B.6).
- 3C 326.1 at $z = 1.8$: for the standard parameters, this source lies at the border of different density enhancements and appears inconclusive (Fig. A.6). Fig. 4 indicates a COD of faint *green* galaxies between 23 and 26 mag, likewise a COD of 24–26 mag galaxies of the *all* sample. Fig. B.7 shows that this source lies between two density enhancements for the sample *all* and at the border of a density enhancement for the sample *green*. The sharp separation for $r_c = 15''$ (top) is lowered for $r_c = 20''$ (bottom). We accept this source as border line cluster and note this in Table D.2.
- 3C 454.1 at $z = 1.8$ (Fig. B.8): for $r_c = 20''$, the map shows that the source lies at the border of a clear *green* COD extending towards the south. However, the attempt to see an overdensity of *red* galaxies on the map fails when using $ct = 1.0$ and the brightness range 23–24 mag indicated in Fig. 5.

These maps corroborate the CODs previously identified from a limited brightness window.

Appendix C: On the OD significance

In Sect. 3.4, we adopted an OD as significant if $\text{abs(OD)} > \text{EoM} = 3\sigma_{\text{SDP}}/\sqrt{N_{\text{ic}}}$ with σ_{SDP} being the standard deviation of the periphery and N_{ic} the number of independent cells in the periphery. Here we illustrate with three examples that this approach is reasonable. Fig. C.1 shows the radial surface density profiles (top row) and histograms (bottom row) from the cell counts for three 3C sources, 3C 210 (good OD), 3C 255 (clear OD but tricky to quantify) and 3C 432 (no OD) as seen on the surface density maps:

- 3C 210: the radial profile declines from the center to the periphery; this holds for both the individual cell counts (“+” signs) and the averaged radial profile (red line with dots). The histogram (bottom row) shows that the distributions of center and periphery are essentially disjoint. This is a clear OD, whatever criterion is used (EoM or $3\sigma_{\text{SDP}}$).
- 3C 255: it appears as a clear OD from the surface density map and the steady decline of the radial profile. However, the radial density shows a “hump” at $r \approx 40\text{--}50''$; there also the error bars increase. Even worse, the histograms of periphery and center overlap, probably due to two effects: there is some other sub-clustering in the periphery, and the central OD is so compact ($<20''$) that it contains also cells with low counts (similar to those in the periphery). This leads to the OD having only a low significance of $N\sigma = 1.9$. This does not satisfactorily account for the physical situation, where it is relevant whether a local density enhancement is centered on the 3C source, irrespective of the presence of other sub-clusterings in the map. On the other hand, EoM yields $S/N = 6.8$, which appears a more realistic description of the OD significance. While for 3C 255 the simple 3σ criterion fails to reveal mathematically the clear visually established OD, the EoM works.
- 3C 432: clear case of no OD, as evident from the maps, radial profiles, and the histograms. This example illustrates that, when using EoM, we do not get an un-justified false OD.

The case of 3C 255 illustrates that one of the main difficulties is to account for the contamination of other sub-clustering in the periphery and of extremely compact central clustering. While there certainly may exist also alternative, sophisticated statistical tools to estimate the whether an OD is significant, we here believe that the simple approach using the EoM serves well.

Appendix D: Tables

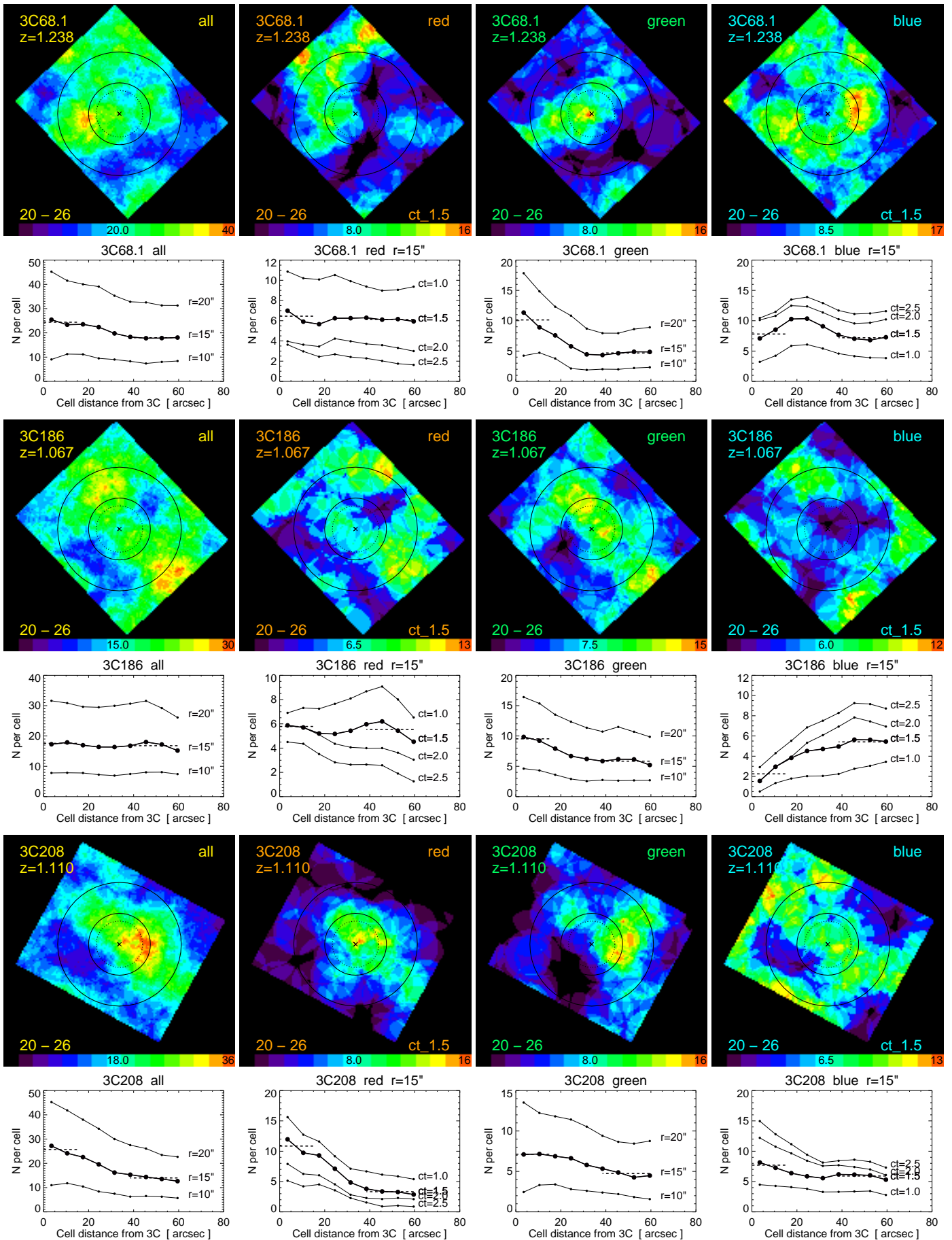


Fig. A.1. Surface density maps and radial density profiles of the remaining 3C fields, similar to 3C210 shown in Fig. 3.

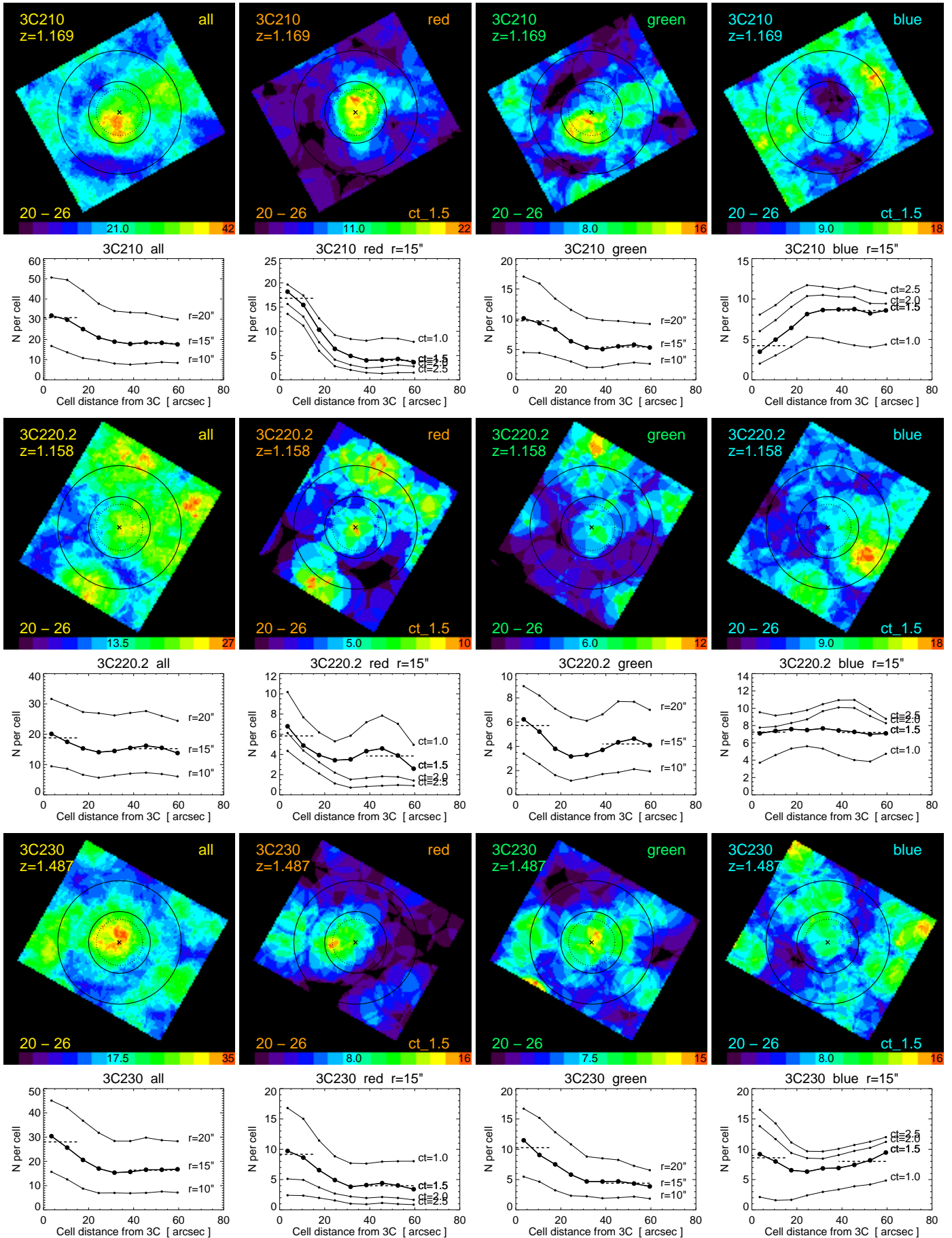


Fig. A.2. Surface density maps and radial density profiles of the 3C fields, continued.

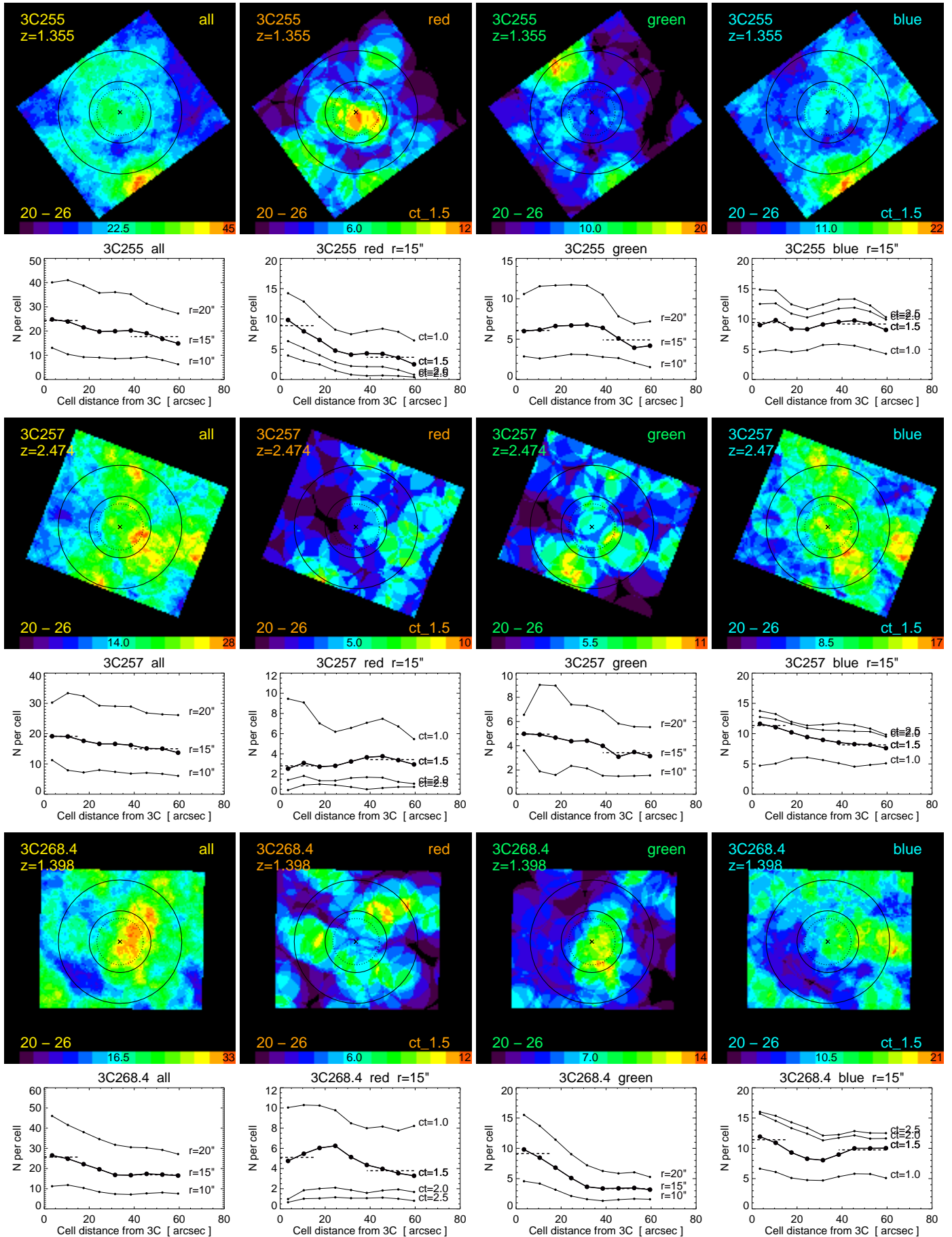


Fig. A.3. Surface density maps and radial density profiles of the 3C fields, continued.

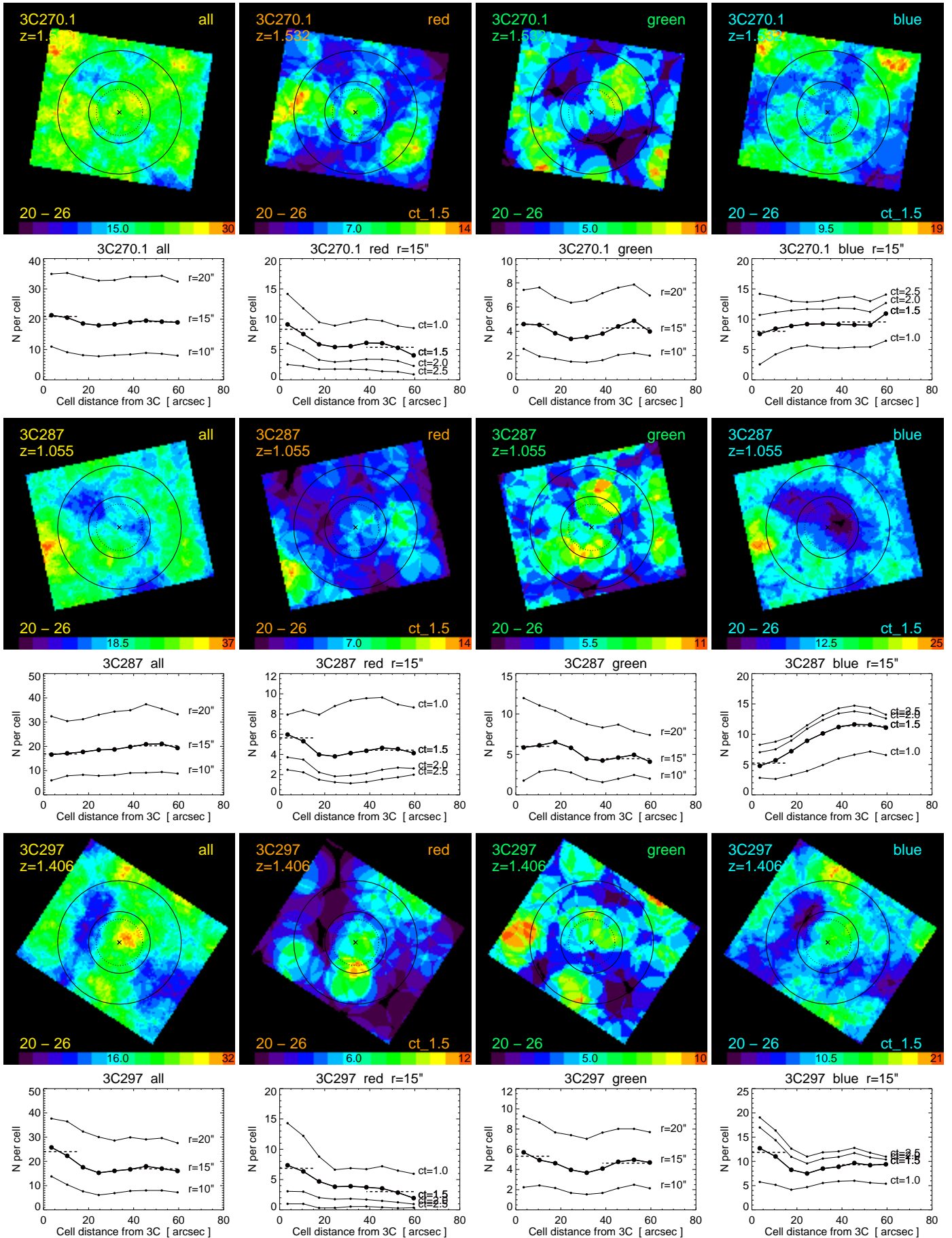


Fig. A.4. Surface density maps and radial density profiles of the 3C fields, continued.

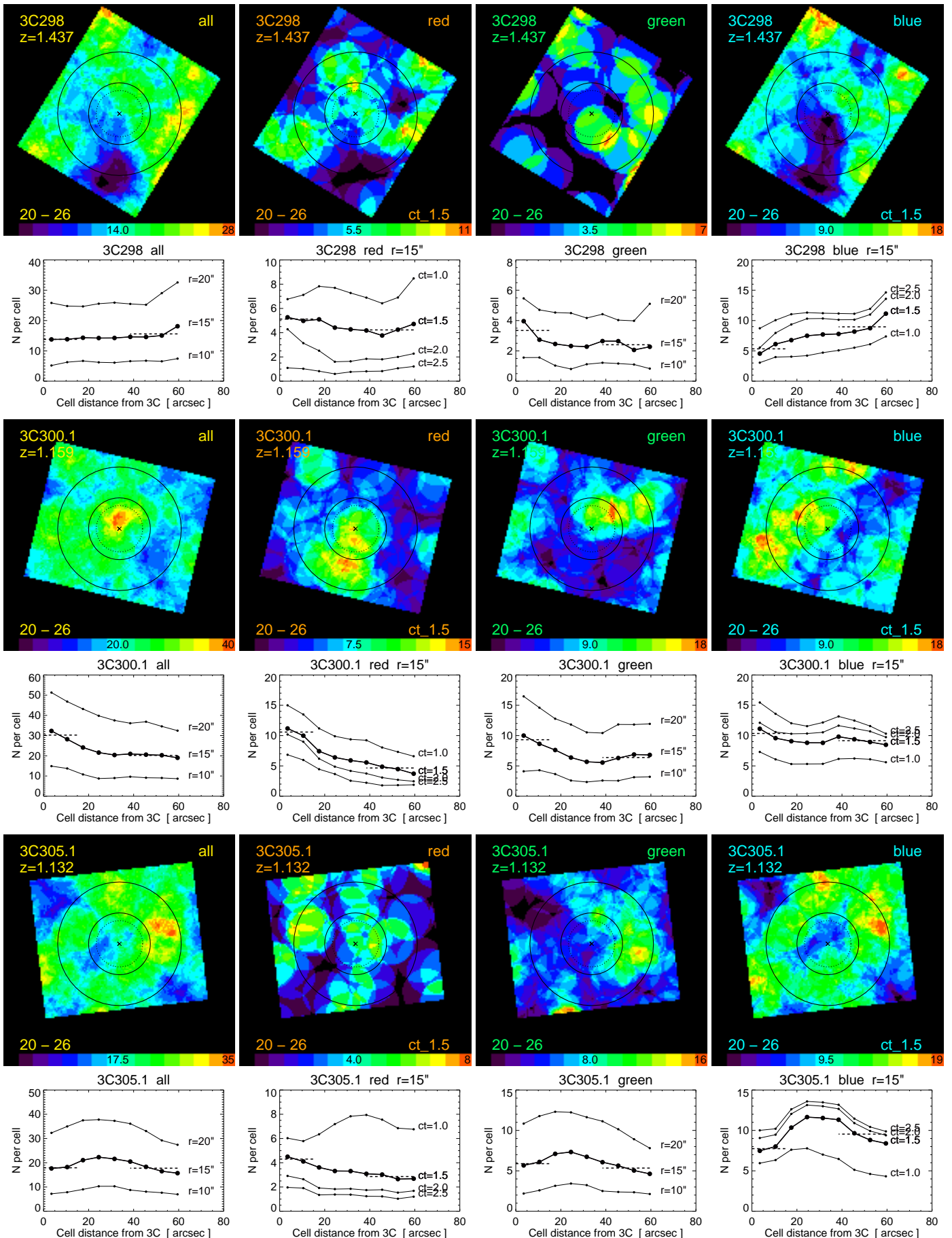


Fig. A.5. Surface density maps and radial density profiles of the 3C fields, continued.

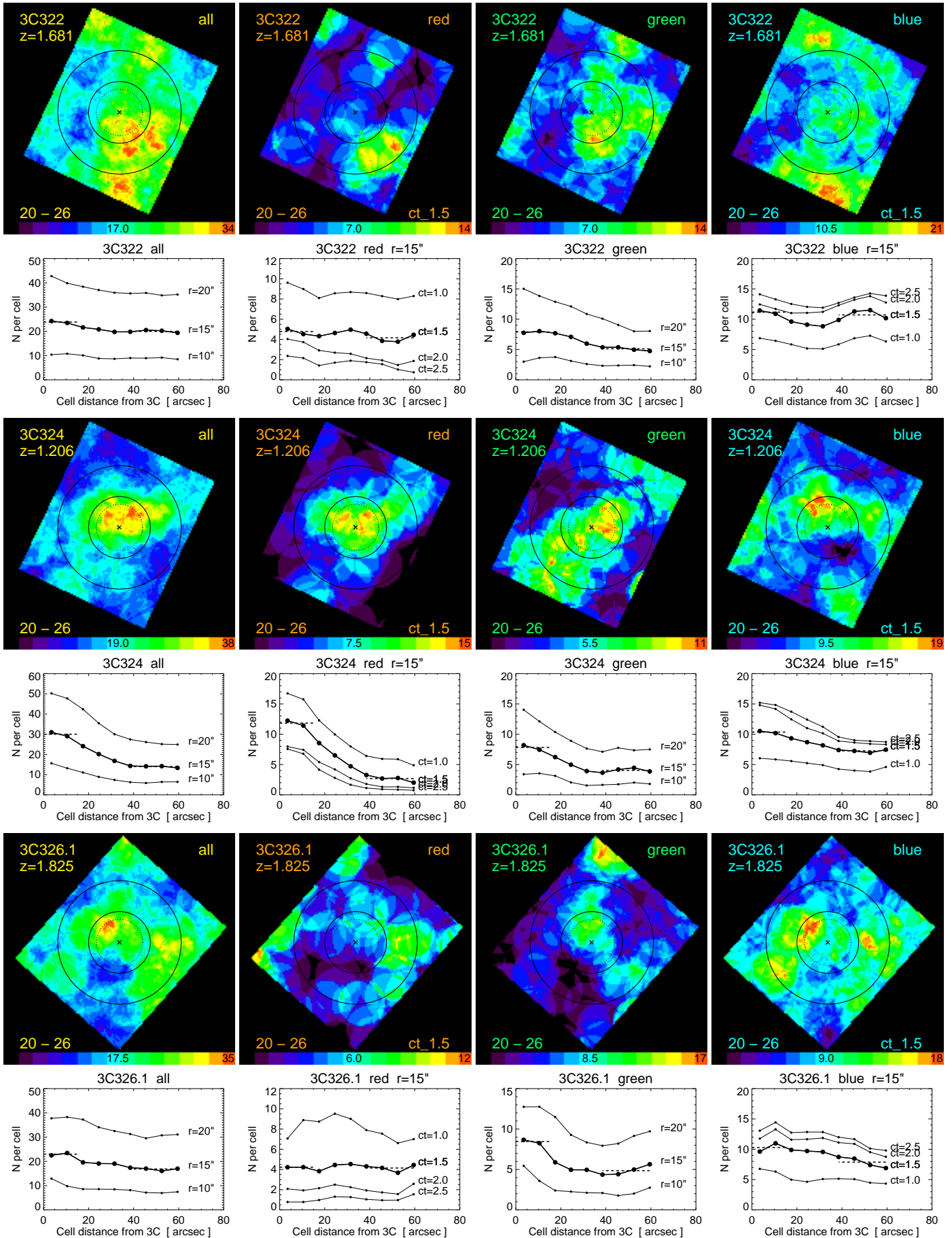


Fig. A.6. Surface density maps and radial density profiles of the 3C fields, continued.

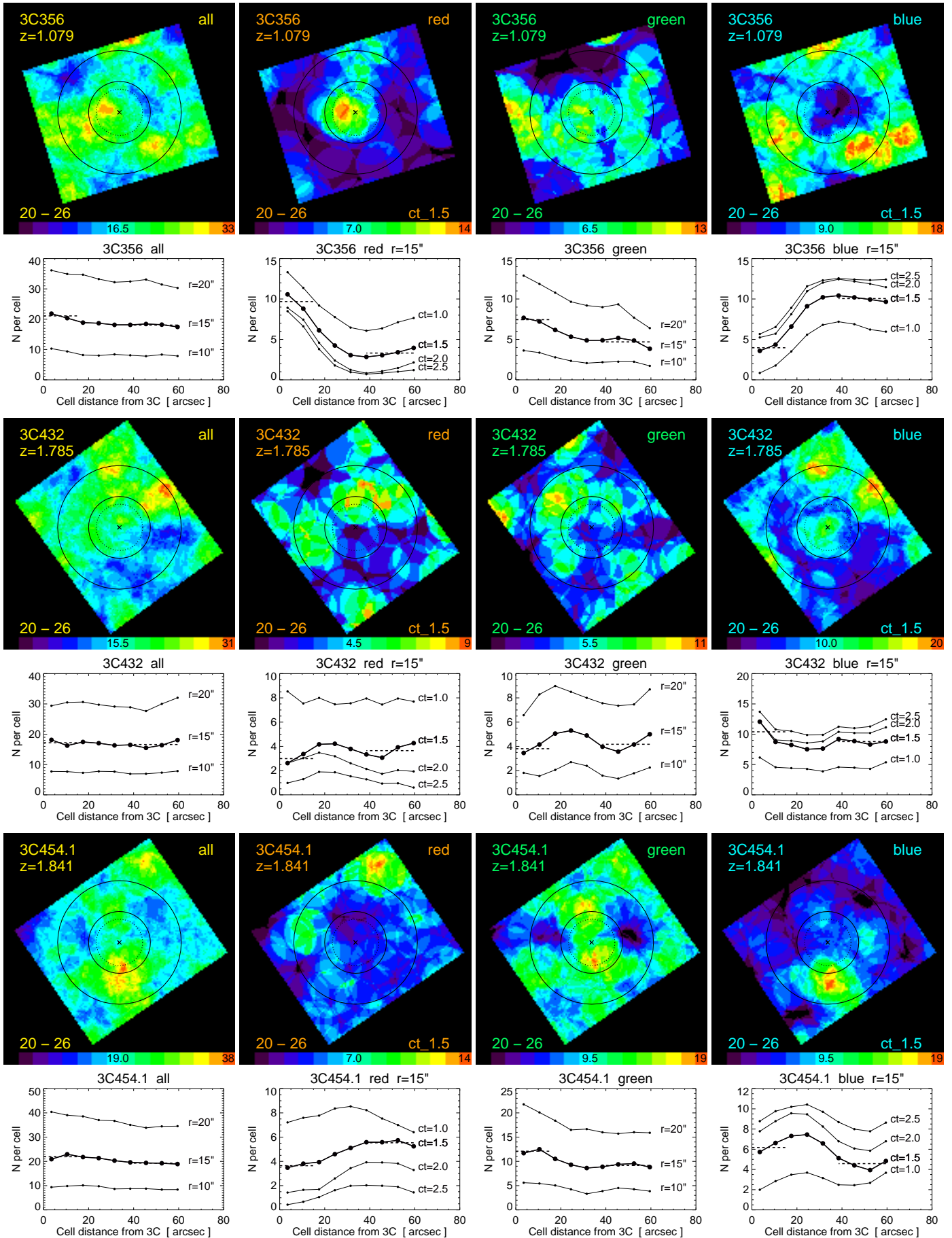
**Fig. A.7.** Surface density maps and radial density profiles of the 3C fields, continued.

Table D.1. Radial surface density profiles, as shown in Figs. A.1 to A.7, using $20 < \text{F140W} < 26$, cell radius $15''$, $ct = 1.5$, and radial bins of $7''$. Column 2 gives the sample color (all, blue, green, red). Columns 3–11 list the average and standard deviation of the number $N(i)$ of galaxies per cell in the i -th radial bin. The i -th radial bin contains all cells whose central position has a distance d from the 3C source of $(i-1) < d/7'' < i$.

(1) Name	(2) color	(3) N1	(4) N2	(5) N3	(6) N4	(7) N5	(8) N6	(9) N7	(10) N8	(11) N9
3C 068.1	all	25.42 ± 3.40	23.35 ± 3.76	23.52 ± 4.61	22.37 ± 6.09	19.78 ± 5.43	18.30 ± 5.28	17.79 ± 5.66	17.84 ± 6.65	18.06 ± 5.34
3C 068.1	red	6.99 ± 2.21	5.91 ± 2.78	5.65 ± 3.21	6.24 ± 3.51	6.25 ± 3.15	6.29 ± 2.95	6.11 ± 3.23	6.16 ± 3.69	5.93 ± 2.68
3C 068.1	green	11.34 ± 2.17	8.91 ± 2.04	7.58 ± 2.20	5.78 ± 2.99	4.45 ± 2.76	4.34 ± 2.01	4.65 ± 1.84	4.88 ± 2.05	4.85 ± 2.27
3C 068.1	blue	7.09 ± 1.45	8.53 ± 2.35	10.28 ± 2.86	10.35 ± 2.39	9.08 ± 2.19	7.67 ± 2.54	7.03 ± 3.03	6.80 ± 2.68	7.27 ± 2.75
3C 186	all	17.26 ± 1.42	17.87 ± 2.67	16.95 ± 3.50	16.36 ± 4.97	16.35 ± 5.10	16.78 ± 4.04	17.99 ± 4.33	17.20 ± 3.38	15.19 ± 2.62
3C 186	red	5.87 ± 0.89	5.70 ± 1.45	5.20 ± 1.75	5.17 ± 1.90	5.43 ± 2.14	5.97 ± 2.51	6.20 ± 2.50	5.44 ± 2.00	4.53 ± 1.60
3C 186	green	9.85 ± 1.55	9.21 ± 2.63	7.91 ± 3.26	6.68 ± 3.01	6.21 ± 2.63	5.86 ± 2.02	6.16 ± 2.37	6.14 ± 2.38	5.22 ± 2.61
3C 186	blue	1.54 ± 0.97	2.96 ± 1.22	3.83 ± 1.22	4.51 ± 1.54	4.71 ± 1.75	4.95 ± 1.77	5.63 ± 2.22	5.62 ± 2.41	5.45 ± 2.61
3C 208.0	all	27.20 ± 3.68	24.16 ± 5.70	22.56 ± 7.42	19.60 ± 7.13	16.19 ± 5.05	15.32 ± 3.93	14.38 ± 3.54	13.56 ± 3.34	12.66 ± 3.07
3C 208.0	red	11.96 ± 1.98	9.74 ± 2.04	9.30 ± 2.24	7.11 ± 2.05	4.84 ± 1.98	3.80 ± 2.13	3.37 ± 2.21	3.28 ± 2.01	2.86 ± 1.72
3C 208.0	green	7.10 ± 2.20	7.16 ± 3.31	6.88 ± 4.46	6.63 ± 4.59	5.79 ± 3.19	5.34 ± 2.36	4.87 ± 1.97	4.27 ± 2.00	4.48 ± 2.04
3C 208.0	blue	8.14 ± 1.26	7.26 ± 1.52	6.38 ± 1.68	5.86 ± 2.03	5.56 ± 2.04	6.18 ± 2.74	6.14 ± 2.92	6.02 ± 2.72	5.31 ± 2.61
3C 210	all	31.79 ± 3.93	29.75 ± 5.05	25.09 ± 5.62	20.88 ± 4.98	18.86 ± 5.20	17.78 ± 5.22	18.39 ± 4.17	18.32 ± 3.43	17.53 ± 3.82
3C 210	red	18.17 ± 1.06	15.44 ± 2.25	10.34 ± 3.32	6.38 ± 2.83	4.92 ± 2.50	4.01 ± 2.02	4.12 ± 2.03	4.30 ± 1.71	3.62 ± 1.31
3C 210	green	10.14 ± 2.55	9.34 ± 3.03	8.34 ± 3.39	6.36 ± 3.41	5.31 ± 2.33	5.06 ± 1.88	5.52 ± 2.20	5.80 ± 2.52	5.33 ± 2.45
3C 210	blue	3.48 ± 1.40	4.97 ± 2.63	6.42 ± 2.39	8.14 ± 2.30	8.63 ± 2.94	8.71 ± 3.16	8.75 ± 2.28	8.22 ± 2.18	8.58 ± 2.22
3C 220.2	all	20.11 ± 2.15	17.49 ± 2.81	15.32 ± 3.43	14.08 ± 3.93	14.48 ± 3.90	15.47 ± 4.30	16.20 ± 4.57	15.51 ± 4.75	13.79 ± 4.58
3C 220.2	red	6.78 ± 1.09	4.88 ± 0.86	3.93 ± 0.99	3.43 ± 1.51	3.51 ± 2.24	4.32 ± 2.32	4.59 ± 2.45	3.89 ± 2.07	2.59 ± 1.47
3C 220.2	green	6.23 ± 0.97	5.21 ± 1.08	3.80 ± 1.42	3.17 ± 1.58	3.29 ± 1.65	3.71 ± 1.60	4.34 ± 2.02	4.63 ± 2.77	4.10 ± 2.99
3C 220.2	blue	7.10 ± 1.62	7.39 ± 1.94	7.59 ± 2.46	7.48 ± 3.24	7.67 ± 3.49	7.44 ± 3.29	7.27 ± 2.67	6.99 ± 1.98	7.10 ± 1.42
3C 230	all	30.40 ± 2.26	25.67 ± 4.02	20.60 ± 4.51	17.04 ± 2.61	15.35 ± 2.90	15.67 ± 4.42	16.55 ± 4.96	16.56 ± 4.29	16.75 ± 3.90
3C 230	red	9.73 ± 1.71	8.63 ± 2.60	6.56 ± 3.29	4.92 ± 2.67	3.82 ± 2.04	4.09 ± 2.35	4.41 ± 2.30	4.03 ± 2.30	3.41 ± 1.87
3C 230	green	11.48 ± 1.46	9.06 ± 1.37	7.51 ± 1.74	5.81 ± 1.89	4.69 ± 1.93	4.67 ± 2.46	4.70 ± 3.02	4.34 ± 2.32	3.87 ± 1.52
3C 230	blue	9.19 ± 0.69	7.99 ± 1.56	6.54 ± 2.28	6.31 ± 2.29	6.84 ± 2.38	6.91 ± 1.77	7.43 ± 2.41	8.18 ± 2.27	9.46 ± 2.76
3C 255	all	24.80 ± 2.20	23.92 ± 3.15	21.51 ± 2.79	19.77 ± 3.19	19.95 ± 3.14	20.22 ± 5.10	19.06 ± 7.43	16.75 ± 6.38	14.88 ± 3.49
3C 255	red	9.83 ± 1.46	7.96 ± 2.44	6.53 ± 2.04	4.77 ± 1.50	4.10 ± 1.47	4.31 ± 2.10	4.24 ± 2.47	3.60 ± 2.55	2.51 ± 1.83
3C 255	green	5.99 ± 1.00	6.16 ± 1.29	6.62 ± 1.39	6.70 ± 2.82	6.76 ± 3.68	6.40 ± 4.31	5.09 ± 3.86	3.93 ± 2.63	4.18 ± 1.32
3C 255	blue	8.98 ± 1.46	9.80 ± 1.41	8.36 ± 1.84	8.30 ± 1.90	9.09 ± 2.51	9.51 ± 2.89	9.73 ± 3.26	9.21 ± 3.03	8.19 ± 2.16
3C 257	all	19.15 ± 1.34	19.06 ± 3.24	17.61 ± 4.49	16.62 ± 4.03	16.61 ± 3.94	16.19 ± 4.28	15.11 ± 3.88	15.03 ± 4.02	13.70 ± 2.61
3C 257	red	2.53 ± 0.80	3.09 ± 1.29	2.73 ± 1.65	2.81 ± 1.53	3.24 ± 1.62	3.66 ± 1.75	3.76 ± 1.64	3.37 ± 1.35	2.95 ± 1.37
3C 257	green	4.99 ± 0.58	4.92 ± 1.31	4.67 ± 1.82	4.38 ± 1.94	4.41 ± 2.21	3.99 ± 2.09	3.09 ± 1.41	3.48 ± 1.54	3.14 ± 1.52
3C 257	blue	11.63 ± 1.34	11.05 ± 1.61	10.21 ± 2.15	9.44 ± 2.22	8.96 ± 2.39	8.54 ± 2.55	8.26 ± 2.67	8.18 ± 2.83	7.61 ± 1.99
3C 268.4	all	26.49 ± 3.10	24.84 ± 4.53	22.15 ± 5.04	19.62 ± 5.16	16.82 ± 4.21	16.69 ± 4.03	17.36 ± 3.61	16.99 ± 3.65	16.49 ± 4.78
3C 268.4	red	4.75 ± 0.84	5.46 ± 1.05	6.04 ± 1.69	6.25 ± 2.35	5.13 ± 2.19	4.35 ± 2.29	3.97 ± 2.18	3.53 ± 1.93	3.28 ± 1.76
3C 268.4	green	9.81 ± 1.42	8.46 ± 2.30	6.81 ± 2.92	5.09 ± 2.72	3.65 ± 1.97	3.37 ± 1.47	3.40 ± 1.69	3.46 ± 2.10	3.18 ± 2.60
3C 268.4	blue	11.93 ± 1.64	10.92 ± 2.54	9.31 ± 3.03	8.28 ± 3.38	8.04 ± 3.58	8.97 ± 3.33	10.00 ± 2.75	9.99 ± 2.34	10.03 ± 2.20
3C 270.1	all	21.31 ± 1.98	20.52 ± 2.48	18.58 ± 2.96	17.98 ± 3.37	18.30 ± 3.08	19.04 ± 3.00	19.52 ± 2.87	19.18 ± 4.07	18.95 ± 4.64
3C 270.1	red	9.14 ± 1.21	7.55 ± 1.43	5.85 ± 1.53	5.41 ± 2.00	5.55 ± 2.31	6.09 ± 2.81	6.03 ± 2.65	5.28 ± 2.24	4.03 ± 2.03
3C 270.1	green	4.60 ± 0.74	4.53 ± 1.59	3.84 ± 2.10	3.38 ± 2.38	3.52 ± 2.06	3.81 ± 1.83	4.41 ± 1.60	4.87 ± 1.79	3.99 ± 1.99
3C 270.1	blue	7.57 ± 0.95	8.44 ± 1.49	8.88 ± 1.73	9.19 ± 2.15	9.23 ± 1.94	9.14 ± 2.30	9.08 ± 2.99	9.03 ± 3.97	10.93 ± 4.63
3C 287	all	16.60 ± 2.06	17.13 ± 2.94	17.70 ± 4.60	18.54 ± 3.99	18.72 ± 3.44	19.79 ± 4.35	20.88 ± 4.65	21.04 ± 4.69	19.32 ± 3.05
3C 287	red	5.97 ± 0.84	5.31 ± 1.12	3.99 ± 1.45	3.81 ± 1.83	4.13 ± 1.80	4.36 ± 1.59	4.65 ± 2.12	4.54 ± 3.06	4.13 ± 2.59
3C 287	green	5.86 ± 1.15	6.13 ± 1.54	6.52 ± 2.33	5.82 ± 2.01	4.46 ± 1.61	4.24 ± 1.75	4.61 ± 1.84	4.95 ± 1.49	4.10 ± 1.27
3C 287	blue	4.78 ± 1.96	5.69 ± 2.49	7.20 ± 2.87	8.91 ± 2.74	10.13 ± 2.37	11.19 ± 2.89	11.62 ± 3.43	11.55 ± 3.03	11.09 ± 2.00
3C 297	all	25.76 ± 2.96	22.30 ± 3.52	17.57 ± 4.47	15.29 ± 5.16	16.08 ± 4.19	16.71 ± 4.35	17.96 ± 5.06	17.02 ± 3.94	16.04 ± 3.06
3C 297	red	7.36 ± 1.03	6.35 ± 1.61	4.69 ± 2.71	3.82 ± 2.53	3.90 ± 2.02	3.73 ± 1.97	3.54 ± 2.07	2.85 ± 1.60	1.94 ± 1.11
3C 297	green	5.70 ± 1.33	4.93 ± 1.80	4.62 ± 1.61	3.96 ± 1.44	3.68 ± 1.89	4.09 ± 2.22	4.76 ± 2.14	4.95 ± 2.10	4.69 ± 1.49
3C 297	blue	12.70 ± 1.35	11.02 ± 2.00	8.26 ± 3.12	7.51 ± 3.14	8.51 ± 2.40	8.89 ± 2.67	9.66 ± 3.57	9.22 ± 3.20	9.41 ± 2.36

Table D.1. continued.

(1) Name	(2) color	(3) N1	(4) N2	(5) N3	(6) N4	(7) N5	(8) N6	(9) N7	(10) N8	(11) N9
3C 298	all	13.78± 2.36	13.83± 3.19	14.32± 3.56	14.23± 3.59	14.26± 4.52	14.62± 5.00	14.59± 5.64	15.05± 5.22	18.13± 3.83
3C 298	red	5.27± 0.78	4.98± 1.30	5.10± 1.34	4.42± 1.72	4.27± 2.28	4.18± 2.42	3.77± 2.29	4.25± 2.31	4.72± 2.08
3C 298	green	3.96± 0.99	2.73± 1.43	2.45± 1.72	2.32± 1.65	2.28± 1.82	2.64± 1.77	2.64± 1.66	2.06± 1.55	2.27± 1.56
3C 298	blue	4.55± 2.47	6.11± 3.22	6.77± 3.31	7.49± 2.56	7.71± 2.36	7.79± 2.64	8.18± 3.49	8.74± 3.58	11.14± 3.20
3C 300.1	all	32.29± 4.31	28.20± 4.70	24.11± 3.68	21.59± 4.07	20.39± 3.69	20.93± 3.51	20.56± 3.96	20.28± 4.62	19.01± 3.72
3C 300.1	red	11.17± 1.31	9.99± 1.96	7.42± 2.49	6.40± 3.39	5.91± 3.14	5.57± 2.54	4.86± 2.15	4.47± 1.95	3.72± 1.85
3C 300.1	green	10.00± 2.05	8.64± 3.64	7.62± 4.26	6.38± 3.25	5.68± 2.83	5.55± 2.84	6.30± 2.22	6.88± 2.09	6.81± 1.82
3C 300.1	blue	11.12± 2.96	9.58± 3.26	9.07± 3.23	8.81± 3.12	8.81± 2.79	9.82± 3.20	9.39± 3.12	8.94± 2.83	8.48± 2.20
3C 305.1	all	17.64± 1.52	18.21± 3.37	21.06± 4.45	22.30± 4.23	21.58± 4.20	20.48± 4.38	18.31± 4.76	16.50± 4.93	15.71± 4.07
3C 305.1	red	4.50± 0.64	4.11± 1.40	3.62± 1.40	3.32± 1.50	3.31± 1.63	3.09± 1.73	3.03± 1.66	2.65± 1.69	2.69± 1.40
3C 305.1	green	5.67± 1.16	6.10± 1.73	7.10± 2.50	7.33± 2.70	6.73± 2.84	6.07± 2.50	5.63± 2.37	5.04± 2.24	4.63± 1.87
3C 305.1	blue	7.48± 1.57	8.01± 1.98	10.35± 2.08	11.65± 2.09	11.53± 2.38	11.32± 2.82	9.65± 3.58	8.81± 3.60	8.39± 3.51
3C 322	all	24.23± 2.25	23.46± 3.85	21.61± 4.83	20.82± 6.25	19.76± 5.71	19.80± 4.66	20.50± 4.35	20.23± 4.68	19.38± 6.09
3C 322	red	5.03± 0.47	4.53± 1.39	4.32± 2.04	4.64± 2.69	4.96± 3.20	4.56± 3.03	3.86± 2.28	3.78± 1.87	4.45± 1.79
3C 322	green	7.76± 1.75	8.03± 2.12	7.69± 2.56	7.09± 2.53	5.97± 2.14	5.37± 2.03	5.37± 2.12	4.97± 1.95	4.75± 1.61
3C 322	blue	11.44± 1.40	10.90± 1.69	9.60± 2.15	9.10± 2.49	8.83± 2.62	9.87± 2.81	11.28± 3.55	11.49± 3.94	10.17± 5.33
3C 324	all	30.95± 2.57	29.05± 5.04	24.09± 5.80	20.17± 4.95	16.81± 4.16	14.32± 3.45	14.12± 3.36	14.19± 3.35	13.34± 2.97
3C 324	red	12.24± 1.11	11.42± 1.50	8.55± 2.00	6.51± 2.24	4.72± 2.18	3.27± 2.10	2.69± 2.06	2.78± 2.24	2.02± 1.89
3C 324	green	8.19± 1.04	7.45± 1.66	6.23± 1.85	4.97± 2.14	3.92± 2.12	3.65± 1.95	4.18± 2.12	4.46± 1.85	3.86± 1.49
3C 324	blue	10.52± 1.83	10.18± 4.24	9.32± 4.99	8.69± 3.49	8.17± 2.36	7.40± 2.26	7.25± 2.73	6.95± 2.83	7.46± 2.41
3C 326.1	all	22.50± 2.71	23.45± 5.01	19.60± 5.53	19.11± 5.23	19.05± 4.22	17.40± 4.37	17.03± 4.20	16.07± 3.35	16.98± 4.77
3C 326.1	red	4.22± 0.94	4.23± 1.49	3.83± 1.89	4.44± 2.27	4.53± 2.13	4.31± 1.90	4.15± 2.16	3.68± 2.24	4.44± 2.85
3C 326.1	green	8.66± 1.34	8.25± 2.39	5.88± 2.69	4.96± 2.51	4.95± 2.23	4.36± 1.86	4.41± 1.96	4.99± 3.11	5.64± 3.88
3C 326.1	blue	9.62± 1.37	10.98± 2.42	9.89± 3.23	9.71± 2.99	9.56± 2.48	8.73± 2.81	8.46± 2.74	7.41± 2.11	6.90± 2.61
3C 356	all	21.83± 3.46	20.36± 4.38	18.87± 4.41	18.67± 4.28	18.14± 4.22	18.15± 4.58	18.42± 4.57	18.20± 3.63	17.45± 4.64
3C 356	red	10.57± 1.35	8.80± 2.60	6.11± 2.37	4.24± 2.10	3.05± 1.77	2.84± 1.99	3.04± 1.75	3.41± 1.55	3.95± 1.73
3C 356	green	7.67± 1.45	7.21± 1.41	6.17± 1.64	5.33± 2.12	4.88± 2.58	4.89± 2.93	5.18± 2.66	4.86± 2.38	3.84± 1.76
3C 356	blue	3.58± 1.26	4.35± 1.57	6.59± 2.26	9.10± 2.94	10.21± 3.22	10.42± 3.11	10.20± 3.16	9.93± 3.03	9.66± 3.96
3C 432	all	18.14± 2.89	16.25± 1.99	17.45± 3.68	17.04± 4.97	16.32± 4.72	16.50± 5.30	15.49± 3.99	16.39± 3.66	18.07± 3.73
3C 432	red	2.62± 1.85	3.36± 1.39	4.17± 1.82	4.22± 2.03	3.79± 1.72	3.34± 1.62	3.07± 1.46	3.92± 1.50	4.27± 1.29
3C 432	green	3.46± 1.01	4.15± 1.16	5.05± 1.48	5.30± 1.60	4.89± 1.88	3.97± 1.52	3.56± 1.38	4.16± 1.88	5.00± 2.23
3C 432	blue	12.07± 1.33	8.73± 1.84	8.24± 1.65	7.52± 2.54	7.64± 3.60	9.19± 4.19	8.86± 3.57	8.31± 2.88	8.80± 2.48
3C 454.1	all	20.91± 2.47	22.93± 4.13	21.77± 5.45	21.35± 6.04	20.31± 5.03	19.60± 3.60	19.37± 3.37	19.22± 4.85	18.90± 6.08
3C 454.1	red	3.48± 0.91	3.81± 1.06	3.94± 1.46	4.60± 1.26	5.11± 1.62	5.58± 1.85	5.58± 2.15	5.74± 2.71	5.24± 2.90
3C 454.1	green	11.70± 1.81	12.50± 2.61	10.51± 3.57	9.31± 4.04	8.62± 3.02	8.89± 2.15	9.39± 2.00	9.55± 2.34	8.82± 2.87
3C 454.1	blue	5.73± 0.78	6.62± 1.65	7.31± 3.09	7.45± 3.89	6.58± 3.73	5.13± 2.96	4.40± 2.17	3.94± 1.60	4.84± 1.54

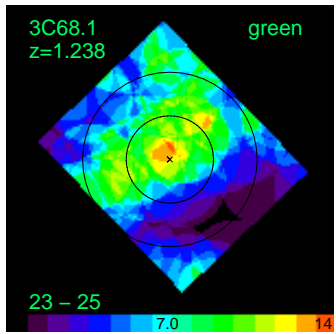


Fig. B.1. Selected surface density maps for 3C 68.1 and 3C 186 made with a cell radius $r_c = 20''$, both showing the COD of green galaxies at $23 < F_{140W} < 25$.

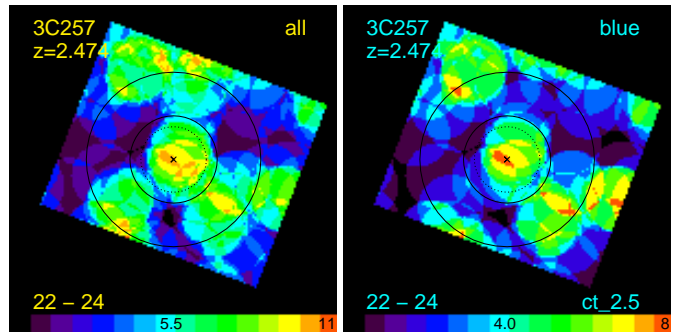


Fig. B.2. Selected surface density maps for 3C 257, showing the COD of galaxies at $22 < F_{140W} < 24$ and bluer than $ct = 2.5$.

Table D.2. Average surface densities for center and periphery and resulting overdensities in units of N galaxies per cell, using $20 < \text{F140W} < 26$, cell radius $15''$, $ct = 1.5$, and radial bins of $7''$. Column 2 gives the sample color (*all*, *blue*, *green*, *red*). Columns 3–4 list the average surface densities for center and periphery. Columns 5–7 list the resulting OD (SD cent – SD peri), the standard deviation (1σ) of the periphery and the significance of the OD in term of $\text{Nsigma} = \text{OD}/\sigma$. Column 8–9 list the uncertainty of the periphery (error of the mean, $\text{EoM} = \sigma/\sqrt{\text{N}_{\text{ic}}}$, adopting $\text{N}_{\text{ic}} = 13$), and the signal/noise (S/N) of the OD. Column 10 lists if a significant OD or UD (negative OD) is present; an OD or UD is significant, if $\text{abs}(\text{S/N}) > 3$ and $\text{abs}(\text{OD}) > 1$. Column 11 lists comments from individual inspection of the density maps in Appendix B. Columns 12–13 list for comparison, if an OD or RS has been found in the studies by K16 (Kotyla et al. 2016), in the row *all* and *red*, respectively, and likewise for G17 (Ghaffari et al. 2017) in the row *red*, if an OD has been found using the IRAC–PSO selection criterion (their Table 5, col. 11).

(1) Name	(2) color	(3) SD cent	(4) SD peri	(5) OD	(6) Sig peri	(7) Nsigma	(8) EoM	(9) S/N	(10) OD/UD	(11) comment	(12) K16	(13) G17
3C 68.1	all	23.85	17.86	5.99	5.98	1.00	1.66	3.61	OD		OD	–
3C 68.1	blue	8.19	6.99	1.19	2.86	0.42	0.79	1.50	–		–	–
3C 68.1	green	9.50	4.77	4.73	2.00	2.36	0.56	8.51	OD		–	–
3C 68.1	red	6.16	6.10	0.07	3.32	0.02	0.92	0.07	–		RS	–
3C 186	all	17.73	17.23	0.50	3.88	0.13	1.08	0.46	–		OD	–
3C 186	blue	2.62	5.60	-2.98	2.36	1.26	0.65	4.55	UD		–	–
3C 186	green	9.36	5.99	3.37	2.44	1.38	0.68	4.98	OD		–	–
3C 186	red	5.74	5.64	0.10	2.28	0.04	0.63	0.16	–		RS	OD
3C 208	all	24.89	13.79	11.10	3.45	3.22	0.96	11.60	OD		OD	–
3C 208	blue	7.47	5.95	1.52	2.82	0.54	0.78	1.95	–		–	–
3C 208	green	7.15	4.59	2.55	2.02	1.27	0.56	4.57	OD		–	–
3C 208	red	10.27	3.25	7.02	2.07	3.40	0.57	12.25	OD		–	OD
3C 210	all	30.23	18.21	12.02	3.87	3.11	1.07	11.20	OD		OD	–
3C 210	blue	4.61	8.53	-3.91	2.25	1.74	0.62	6.27	UD		–	–
3C 210	green	9.53	5.59	3.94	2.37	1.66	0.66	6.00	OD		–	–
3C 210	red	16.09	4.10	11.99	1.83	6.57	0.51	23.67	OD		RS	OD
3C 220.2	all	18.12	15.54	2.57	4.72	0.55	1.31	1.97	–		–	–
3C 220.2	blue	7.32	7.14	0.18	2.26	0.08	0.63	0.29	–		–	–
3C 220.2	green	5.46	4.40	1.05	2.49	0.42	0.69	1.53	–	RS, at OD border	–	–
3C 220.2	red	5.34	4.00	1.34	2.29	0.58	0.64	2.11	–	RS, between 2 ODs	–	OD
3C 230	all	26.81	16.58	10.22	4.55	2.25	1.26	8.10	OD		–	–
3C 230	blue	8.28	8.04	0.23	2.53	0.09	0.70	0.34	–		–	–
3C 230	green	9.63	4.43	5.20	2.59	2.01	0.72	7.24	OD		–	–
3C 230	red	8.89	4.10	4.79	2.26	2.12	0.63	7.65	OD		RS	–
3C 255	all	24.14	17.50	6.64	6.71	0.99	1.86	3.57	OD		–	–
3C 255	blue	9.61	9.28	0.33	3.06	0.11	0.85	0.39	–		–	–
3C 255	green	6.13	4.51	1.61	3.17	0.51	0.88	1.84	–		–	–
3C 255	red	8.41	3.71	4.70	2.48	1.89	0.69	6.83	OD		RS	–
3C 257	all	19.08	14.83	4.25	3.77	1.13	1.05	4.06	OD		–	–
3C 257	blue	11.19	8.11	3.08	2.63	1.17	0.73	4.22	OD		RS	–
3C 257	green	4.93	3.24	1.69	1.49	1.14	0.41	4.11	OD		–	–
3C 257	red	2.95	3.48	-0.52	1.53	0.34	0.42	1.23	–		–	–
3C 268.4	all	25.23	17.08	8.14	3.85	2.11	1.07	7.62	OD		OD	–
3C 268.4	blue	11.15	10.00	1.15	2.52	0.46	0.70	1.65	–		–	–
3C 268.4	green	8.78	3.39	5.39	2.02	2.67	0.56	9.63	OD		–	–
3C 268.4	red	5.30	3.69	1.60	2.04	0.78	0.57	2.83	–		–	–
3C 270.1	all	20.70	19.30	1.40	3.68	0.38	1.02	1.38	–		–	–
3C 270.1	blue	8.23	9.37	-1.14	3.74	0.30	1.04	1.10	–		–	–
3C 270.1	green	4.54	4.51	0.04	1.77	0.02	0.49	0.08	–		–	–
3C 270.1	red	7.93	5.42	2.50	2.51	1.00	0.70	3.59	OD		–	–
3C 287	all	17.00	20.68	-3.68	4.48	0.82	1.24	2.96	–		–	–
3C 287	blue	5.47	11.51	-6.03	3.09	1.95	0.86	7.04	UD		–	–
3C 287	green	6.06	4.65	1.41	1.66	0.85	0.46	3.07	OD		weak OD	–
3C 287	red	5.46	4.52	0.94	2.58	0.37	0.71	1.32	–		–	–

Table D.2. continued.

(1) Name	(2) color	(3) SD cent	(4) SD peri	(5) OD	(6) Sig peri	(7) Nsigma	(8) EoM	(9) S/N	(10) OD/UD	(11) comment	(12) K16	(13) G17
3C 297	all	23.13	17.29	5.83	4.44	1.31	1.23	4.74	OD		–	–
3C 297	blue	11.42	9.46	1.96	3.26	0.60	0.90	2.17	–		–	–
3C 297	green	5.11	4.81	0.30	2.03	0.15	0.56	0.53	–		–	–
3C 297	red	6.59	3.02	3.57	1.87	1.91	0.52	6.90	OD		–	–
3C 298	all	13.81	15.36	-1.55	5.37	0.29	1.49	1.04	–		–	–
3C 298	blue	5.74	8.88	-3.14	3.63	0.87	1.01	3.12	OD	marginal	–	–
3C 298	green	3.03	2.37	0.66	1.63	0.41	0.45	1.46	–		–	–
3C 298	red	5.04	4.10	0.94	2.29	0.41	0.64	1.48	–		–	–
3C 300.1	all	29.18	20.20	8.98	4.21	2.13	1.17	7.70	OD		OD	–
3C 300.1	blue	9.95	9.08	0.87	2.90	0.30	0.81	1.08	–		–	–
3C 300.1	green	8.97	6.59	2.38	2.13	1.12	0.59	4.02	OD		–	–
3C 300.1	red	10.27	4.53	5.74	2.07	2.77	0.57	9.98	OD		RS	OD
3C 305.1	all	18.08	17.22	0.86	4.83	0.18	1.34	0.64	–		–	–
3C 305.1	blue	7.88	9.14	-1.25	3.61	0.35	1.00	1.25	–		–	–
3C 305.1	green	6.00	5.25	0.75	2.28	0.33	0.63	1.19	–		–	–
3C 305.1	red	4.20	2.83	1.36	1.64	0.83	0.46	3.00	OD	marginal	–	–
3C 322	all	23.64	20.21	3.44	4.81	0.71	1.34	2.57	–		OD	–
3C 322	blue	11.03	11.16	-0.13	4.06	0.03	1.13	0.12	–		–	–
3C 322	green	7.97	5.12	2.85	2.00	1.43	0.55	5.14	OD	at border of OD	–	–
3C 322	red	4.65	3.93	0.72	2.07	0.35	0.58	1.25	–		–	OD
3C 324	all	29.52	14.02	15.51	3.31	4.69	0.92	16.90	OD		OD	–
3C 324	blue	10.27	7.17	3.10	2.73	1.14	0.76	4.09	OD		–	–
3C 324	green	7.63	4.23	3.40	1.94	1.75	0.54	6.32	OD		–	–
3C 324	red	11.62	2.61	9.01	2.12	4.26	0.59	15.35	OD		–	OD
3C 326.1	all	23.23	16.67	6.55	4.05	1.62	1.12	5.83	OD	between 2 ODs	OD	–
3C 326.1	blue	10.66	7.82	2.84	2.59	1.10	0.72	3.96	OD		–	–
3C 326.1	green	8.34	4.83	3.51	2.84	1.24	0.79	4.46	OD		–	–
3C 326.1	red	4.23	4.03	0.20	2.34	0.09	0.65	0.31	–		–	OD
3C 356	all	20.70	18.18	2.53	4.28	0.59	1.19	2.13	–		–	–
3C 356	blue	4.17	10.01	-5.84	3.27	1.79	0.91	6.45	UD		–	–
3C 356	green	7.32	4.84	2.48	2.47	1.00	0.69	3.62	OD		–	–
3C 356	red	9.22	3.33	5.89	1.71	3.45	0.47	12.44	OD		–	–
3C 432	all	16.70	16.25	0.46	3.94	0.12	1.09	0.42	–		–	–
3C 432	blue	9.53	8.65	0.88	3.17	0.28	0.88	1.00	–		–	–
3C 432	green	3.99	4.02	-0.03	1.81	0.02	0.50	0.06	–		–	–
3C 432	red	3.18	3.58	-0.39	1.53	0.26	0.42	0.93	–		–	–
3C 454.1	all	22.44	19.24	3.20	4.49	0.71	1.24	2.57	–		OD	–
3C 454.1	blue	6.41	4.31	2.10	1.91	1.10	0.53	3.97	OD	at border of OD	–	–
3C 454.1	green	12.30	9.35	2.95	2.30	1.28	0.64	4.62	OD		–	–
3C 454.1	red	3.72	5.58	-1.86	2.51	0.74	0.70	2.67	–		–	OD

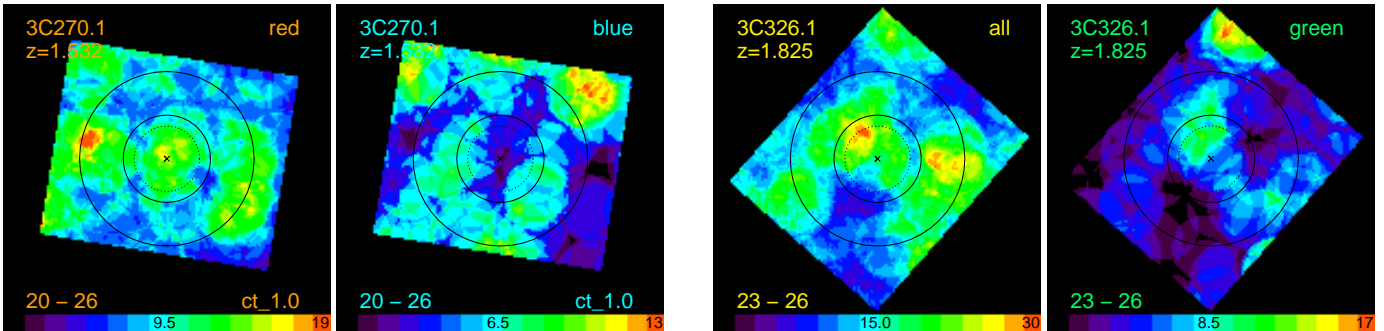


Fig. B.3. Selected surface density maps for 3C 270.1, showing the COD of galaxies at $20 < F_{140W} < 26$ and redder than $ct = 1.0$.

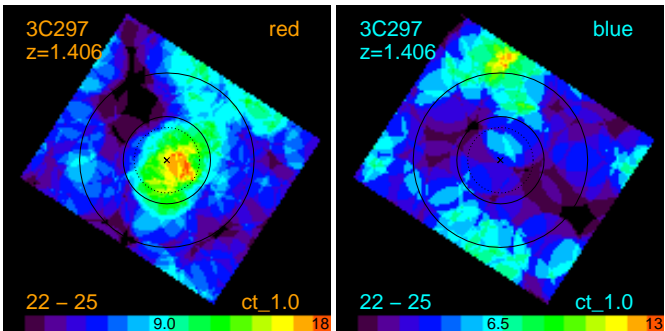


Fig. B.4. Selected surface density maps for 3C 297, showing the COD of galaxies at $22 < F_{140W} < 25$ and redder than $ct = 1.0$.

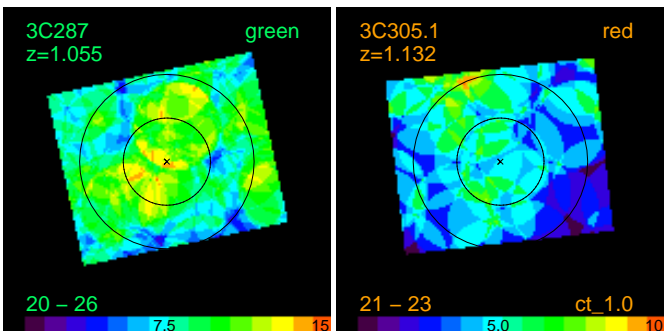


Fig. B.5. Selected surface density maps for 3C 287 and 3C 305.1 for cell radius $r_c = 20''$, showing the clustering of green galaxies near 3C 287, but no red clustering for 3C 305.1.

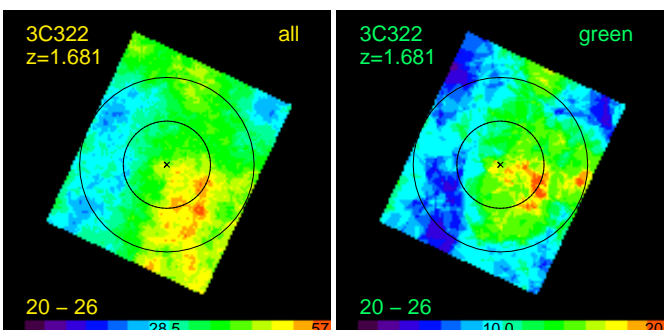


Fig. B.6. Selected surface density maps for 3C 322, showing that this source lies at the clustering border of green galaxies and all galaxies for cell radius $r_c = 20''$.

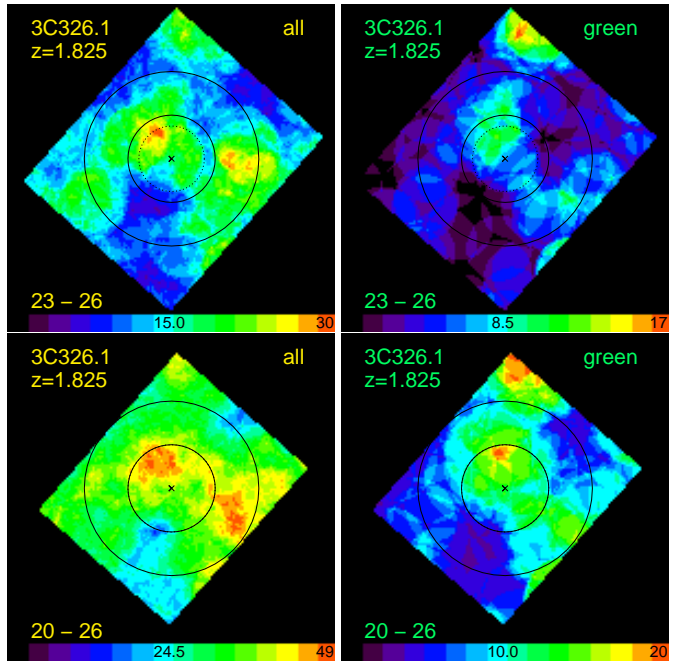


Fig. B.7. Selected surface density maps for 3C 326.1, showing that this source lies between two density enhancements of green galaxies and all galaxies, at suited brightness cuts for cell radius $r_c = 15''$ (top) and for cell radius $r_c = 20''$ (bottom).

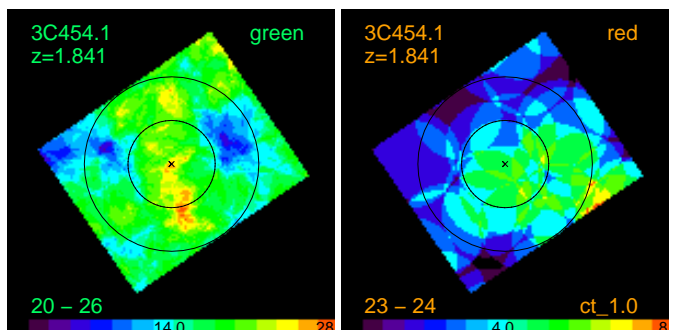


Fig. B.8. Selected surface density maps for 3C 454.1 for cell radius $r_c = 20''$, showing the clustering of green galaxies, but not of red galaxies for the limited brightness range and $ct = 1.0$.

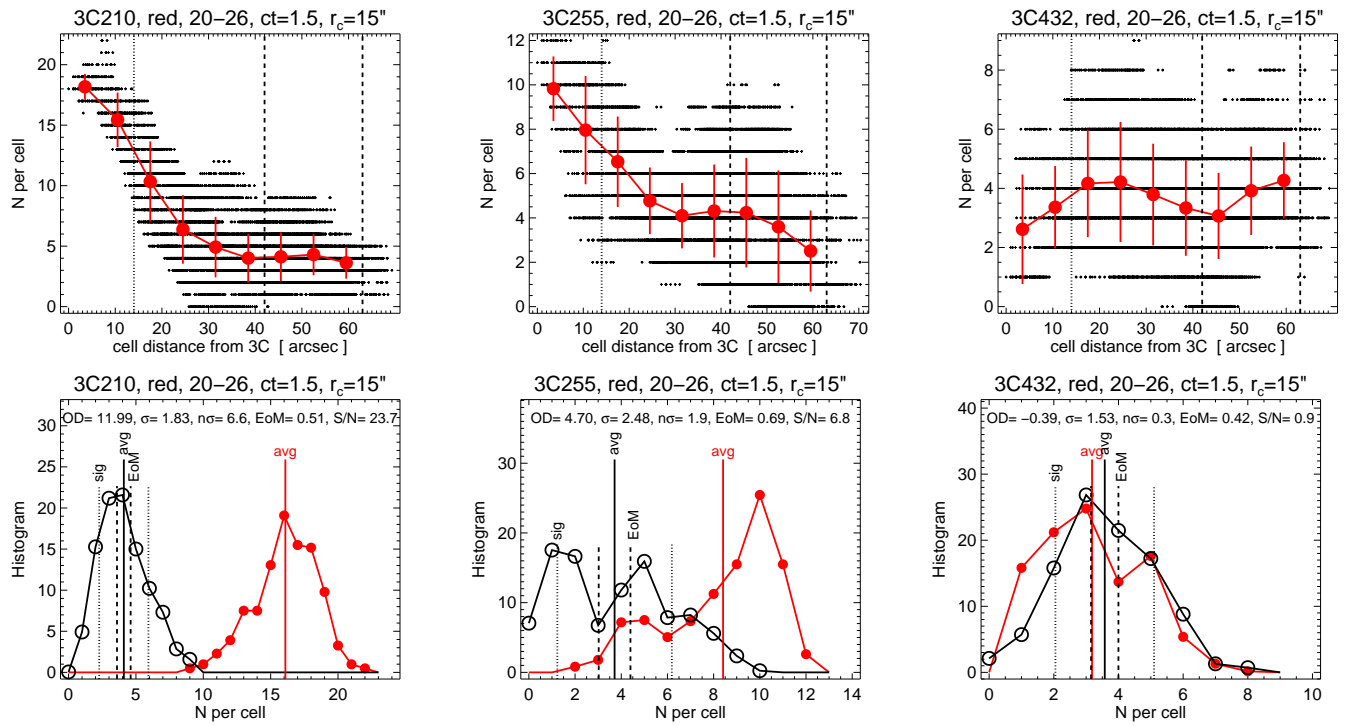


Fig. C.1. Radial surface density profiles and histograms from the cell counts for three 3C sources, using standard parameters. Top: individual cells marked with small "+" symbols and mean radial profile in red with fat dots. The vertical dotted and dashed lines mark the radial limits used for the statistics of center and periphery. Bottom: histogram of the cell counts (made from the "+" in the top row), red with fat dots for center, black with circles for periphery. The vertical lines mark the average (avg), and for periphery also standard deviation (1σ) and the uncertainty (= error of the mean, EoM = $\sigma/\sqrt{13}$), i.e. assuming $N_{ic} = 13$ independent cells in the periphery). The statistics numbers are written in the top of the histogram.